ROTATING LINE CAMERAS: EPIPOLAR GEOMETRY AND SPATIAL SAMPLING

By

Fay Huang

Shou Kang Wei

and

Reinhard Klette

INSTITUTE FOR MATHEMATICS AND ITS APPLICATIONS
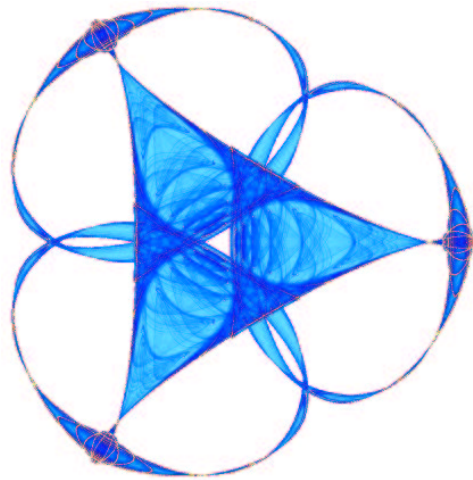
Rotating Line Cameras:
Epipolar Geometry and Spatial Sampling

Fay Huang, Shou Kang Wei, and Reinhard Klette

Taipei and Auckland

Abstract. Rotating line cameras project 3D scenes on a cylindric surface, where one or multiple rotating sensor lines allow to compose panoramic images line by line. An important special case of such a camera is defined by two lines with symmetric viewing angles with respect to the cylinder's surface normal. The report analyzes epipolar geometry for the general case of such rotating line cameras, and discusses spatial distributions of (potential) 3D samples for the special symmetric camera architecture.

STEREO PANORAMAS

Various camera architectures [see (Daniilides and Papanikolopoulos, 2004; Daniilides and Klette, 2006)] serve in machine vision as visual perceptive devices for computers or robots. Applications often demand particular quality parameters such as color accuracy, very high resolution, minimized radial distortion, and so forth. Panoramic images became widely popular just a few years ago [starting with (Chen, 1995) or (Szeliski and Kang, 1995)], and stitching-based panorama generation is today a common technique for home, commercial, or professional photography.

Many applications demand more than just stitching of multiple "pinhole-type" images. As a first example, robotics requires typically dynamic (often very fast), "approximately geometrically correct" omnidirectional vision, but possibly just with low or medium image resolution. The quality of close-range photogrammetry (e.g., for static scenes of architecture) depends on image resolution to support very accurate representations of scene geometry. Computer animations in a professional context often specify increased needs for resolution, photometric correctness, or geometric accuracy.

The interest of the authors in panoramic images was at first (in the late 1990s) directed on improving the performance of 3D scene animations for a wide consumer market. This can be achieved by allowing stereo-viewing, independent (possibly interactive) animations of 3D objects within a panoramic scene (e.g., just waving of leaves, or random drives of cars through a scene), flexible moves between different view points, or special effects such as illumination changes in a panoramic scene (e.g., a sunset).

Report (Wei et al., 1998a) introduced a new panorama visualization approach, based on a general optimization of color filters for full-color anaglyph stereoscopic viewing. Panoramic and anaglyphic (i.e., stereo-viewable) image acquisition setups are incompatible intrinsically; the report proposed an error measure for anaglyphic panoramic images and provided a formula for controlling this error, allowing to adjust the camera positioning at the time of photo shooting. The report also described a real-time interactive player for navigation in a stereo panoramic virtual world, with

anaglyphic panoramic images taken at different viewpoints. The player came with a directional indicator (a "map" of the scene around the viewpoints, similar to QuickTimeVR's environment maps), auto-spin options, and (most interesting) manipulable objects embedded into the stereo panorama. [This is just to illustrate the starting point of the authors when entering into the panoramic imaging field.] The figure below shows the interface of this 1998 interactive player of stereo panoramas (note: it requires anaglyphic eyeglasses for proper stereo viewing): the directional indicator is on the left, and the bottom line of the dialog box informs that the globe is available for interactive manipulation (i.e., rotation).
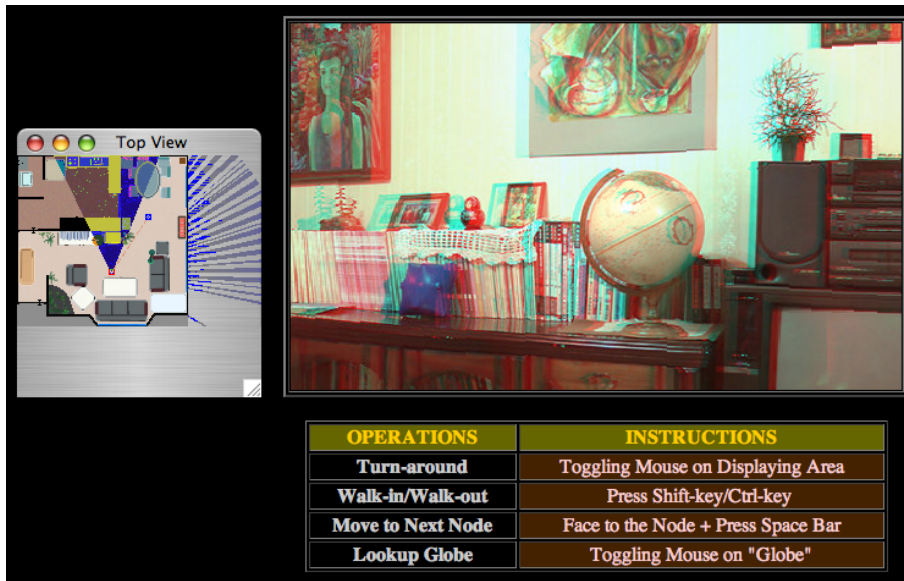
Panoramas were still generated by stitching in this 1998 project, and they had inherent geometric inaccuracies. Theoretical studies pointed out that the use of a rotating line camera [which was at this time an abstraction of the approach by (Peleg and Herman, 1997) where panoramas were created by selecting columns in subsequent video frames] would allow to overcome geometric inaccuracies of projected scenes. As it turned out, stereo viewing can also be based (to some extend) on monocular images [see (Wei et al., 1999a)], but the generation of a directional indicator requires a geometric reconstruction of the 3D scene [see textbooks such as (Hartley and Zisserman, 2000) or (Faugeras and Luong, 2001)]. The general direction in our research is about the use of rotational line cameras for stereo reconstruction and stereo viewing.

In 1998 the authors were informed that line cameras, designed for pushbroom applications (i.e., digital aerial photography), already had been

positioned and rotated on tripods, generating panoramas this way. The predecessor of the WAOSS/HRSC camera [described in (Reulke and Scheele, 1998)], the Wide Angle Airborne Camera WAAC, was used in 1995 for taking the first panoramic image (a view from the roof of Dornier in Germany) using a rotating line camera; see the figure below.

This image is of very high resolution; each column is composed of more than 5,000 pixels. Another panoramic image from 1995, also taken by the rotating WAAC, shows a square in the Eastern part of Berlin.

The authors thank Professors Ralf Reulke and Herbert Jahn from DLR Berlin for the permission to reproduce the two panoramic images above and for providing a very high-resolution rotating line camera for experiments [which will (also) be reported in this report]. The authors thank both, and also Karsten Scheibe and Drs. Anko Börner and Martin Scheele for continuous interest, many discussions, and all kinds of support.

The used cameras had up to 10,000 color pixels in rotating line sensors. Panoramic images of this resolution are today required (e.g.) for texture mapping of 3D surfaces generated based on surface points acquired by a laser range finder (at multiple view points); see (Klette and Reulke, 2005) and (Klette and Scheibe, 2005).

For the theoretical model of rotating line cameras, see (Huang, et al. 2006). This report uses exactly the same notations as defined in (Huang, et al. 2006), and we will not redefine those notations in this report.

EPIPOLAR GEOMETRY

Epipolar geometry characterizes the geometric relationships between optical centers of two cameras, a point in 3D space, and its potential position in both images. A benefit of knowing the epipolar geometry is that if given any point in one of both images (showing the projection of a point in 3D space), epipolar geometry defines a parameterized (i.e., Jordan) curve γ (the *epipolar curve*) of possible locations of the corresponding point (if visible at all) in the other image. The parameter t of the curve $\gamma(t)$ then allows in computational stereo to 'move' along the curve when testing image points for actual correspondence. Interest in epipolar geometry is also motivated by *stereo viewing*[1]. There is a 'preferred' epipolar geometry which supports depth perception, and this is defined by parallel *epipolar lines*; these lines are a special case of epipolar curves.

The epipolar geometry of two pinhole cameras defines epipolar lines, but these are in general not all parallel in each of the two image planes. The epipolar geometry of two panoramic cameras defines Jordan curves on cylinders, and we will also identify the case where two panoramic images support depth perception.

Computational stereo with images of the scale of large panoramic images (say, 10,000 times 100,000 pixels) definitely requires the knowledge of epipolar curves for allowing reasonably sized search spaces for corresponding points. This ensures not only efficiency in stereo matching, but also a decrease of the probability of false matching.

Epipolar geometry is widely studied and applied for pinhole cameras,[2] and there is an increasing interest in stereo analysis for multiple planar images. Shape from motion, novel few synthesis (image-based rendering),

---

[1] Different techniques are used since 1838 (Sir Charles Wheatstone; his 'stereopticon' was demonstrated for line drawings, and a year later for photographs) for depth perception by showing one image to the left, and the other image to the right eye, either in parallel or in alternations.

[2] See computer vision text books, such as (Faugeras, 1993; Xu and Zhang, 1996; Klette et al., 1998; Hartley and Zisserman, 2000; Faugeras and Luong, 2001).

ego-motion analysis, or object recognition and localization are examples of related applications; see, for example, (Xu and Zhang, 1996; Kanatani, 1993; Laveau and Faugeras, 1994; Zhang et al., 1994; Zhang and Xu, 1997; Evers-Senne et al., 2004; Liu et al., 2005). Compared with the pinhole case, there is much less work reported so far for panoramic cameras.

Approaches computing epipolar curves in panoramic images were often focused on single-center panoramas; see, for example, (McMillan and Bishop, 1995a) for image-based rendering applications. (Svoboda, 1999) addressed the epipolar geometry of a central panoramic pair using catadioptric camera. This chapter presents a unified approach for computing epipolar curves for the general case of polycentric panoramas [as published in short form in (Huang et al., 2001b)].

The epipolar geometry of a pair of symmetric panoramas, which is a special case of polycentric panoramas, has been studied in (Shum et al., 1999; Shum and Szeliski, 1999). In this case the epipolar curves become straight lines (assuming the surface of the cylinder is unfolded onto a rectangle) and coincide with image rows. (Seitz, 2001) specifies all possible epipolar surfaces as a subset of doubly-ruled surfaces[3] that allow a generation of images suitable for stereo vision. In our case of a cylindric stereo-panoramic pair, the epipolar surface is a half-hyperboloid.

Section 2.1 states a epipolar curve equation theorem and its proof for the general case of polycentric panoramas. Specific cases (such as leveled or symmetric panoramas) are discussed in Section 2.2.

2.1. General Epipolar Curve Equation

We consider an arbitrary pair of polycentric panoramas $E_{\mathcal{P}_1}(R_1, f_1, \omega_1, \gamma)$ and $E_{\mathcal{P}_2}(R_2, f_2, \omega_2, \gamma)$, where R, f, ω, and γ are the camera parameters specifying off-axis distance, effective focal length, principal angle, and angular unit. Subscripts $_1$ and $_2$ are used to indicate that parameters may differ from one panorama to the other.

A polycentric panoramic pair defines a *general epipolar curve equation* because the epipolar geometry of other types of cylindric panoramic pairs can be derived from this equation (as described later).

Given is an image point $\mathbf{p}_1$ with image coordinates (x_1, y_1) on $E_{\mathcal{P}_1}$. This image point is a projection of an (unknown) point in 3D space, which (assuming it is visible) will project into the *corresponding* image point $\mathbf{p}_2$ in $E_{\mathcal{P}_2}$. Without knowing the projected 3D point, the knowledge about camera parameters and $\mathbf{p}_1$ allows to specify the possible locations of $\mathbf{p}_2$.

---

[3] The only doubly-ruled surfaces in 3D space are the plane, the hyperboloid, and the hyperbolic paraboloid (Hilbert and Cohn-Vossen, 1932).

This point has image coordinates (x_2, y_2) on $E_{\mathcal{P}_2}$. We also call sometimes panorama $E_{\mathcal{P}_1}$ the *source image*, and panorama $E_{\mathcal{P}_2}$ the *destination image*, and use 'source' or 'destination' for other components in the same sense.

The origin of the source camera coordinate system is denoted by $\mathbf{O}_1$, and for the destination camera coordinate system by $\mathbf{O}_2$. Assume that the 3×3 rotation matrix $\mathbf{R}_{\mathbf{o}_1\mathbf{o}_2}$ and the 3×1 translation vector $\mathbf{T}_{\mathbf{o}_1\mathbf{o}_2}$ specify orientation and position of the destination camera coordinate system with respect to the source camera coordinate system. The rotation matrix $\mathbf{R}_{\mathbf{o}_1\mathbf{o}_2}$ is decomposed into its three row vectors $[\mathbf{r}_1^T \mathbf{r}_2^T \mathbf{r}_3^T]^T$, and the translation vector is represented by its three elements t_x, t_y, t_z. The general epipolar curve theorem is stated as follows.

THEOREM 2.1. *Let (x_1, y_1) and (x_2, y_2) denote the image coordinates of the projection of a 3D point in the source image $E_{\mathcal{P}_1}$ and the destination image $E_{\mathcal{P}_2}$, respectively. Consider x_1 and y_1 as being given. Let $\alpha_1 = \frac{2\pi x_1}{\mu W_1}$, $\alpha_2 = \frac{2\pi x_2}{\mu W_2}$, $\delta_1 = (\alpha_1 + \omega_1)$, $\delta_2 = (\alpha_2 + \omega_2)$, and $\beta_1 = \arctan(\frac{y_1}{f_1})$. The corresponding epipolar curve on the destination image $E_{\mathcal{P}_2}$ can be represented by the equation*

$$y_2 = \frac{f_2 \boldsymbol{r}_2^T \cdot \boldsymbol{V}}{\sin \delta_2 \boldsymbol{r}_1^T \cdot \boldsymbol{V} + cos\delta_2 \boldsymbol{r}_3^T \cdot \boldsymbol{V} - R_2 \cos \omega_2},$$

which is only valid if the value of the denominator is greater than zero. The vector $\boldsymbol{V}$ is defined as follows:

$$\boldsymbol{V} = \boldsymbol{A} + \frac{R_2 \sin \omega_2 + \cos \delta_2 \boldsymbol{r}_1^T \cdot \boldsymbol{A} - \sin \delta_2 \boldsymbol{r}_3^T \cdot \boldsymbol{A}}{\sin \delta_2 \boldsymbol{r}_3^T \cdot \boldsymbol{B} - \cos \delta_2 \boldsymbol{r}_1^T \cdot \boldsymbol{B}} \boldsymbol{B},$$

where

$$\boldsymbol{A} = \begin{bmatrix} R_1 \sin \alpha_1 - t_x \\ -t_y \\ R_1 \cos \alpha_1 - t_z \end{bmatrix} \quad and \quad \boldsymbol{B} = \begin{bmatrix} \sin \delta_1 \cos \beta_1 \\ \sin \beta_1 \\ \cos \delta_1 \cos \beta_1 \end{bmatrix}$$

Furthermore, the matrix $[\boldsymbol{r}_1^T \boldsymbol{r}_2^T \boldsymbol{r}_3^T]^T$ and the vector $[t_x, t_y, t_z]^T$ specify the orientation and the position of the panoramic camera of $E_{\mathcal{P}_2}$ with respect to the camera coordinate system of the panoramic camera of $E_{\mathcal{P}_1}$.

Proof Image point $\mathbf{p}_1$ with image coordinates (x_1, y_1) on $E_{\mathcal{P}_1}$ defines a 3D projection ray, denoted as $\mathcal{L}$. Let $\mathbf{C}_1$ denote the optical center associated with image column x_1. The projection ray $\mathcal{L}$ emits from $\mathbf{C}_1$ and is incident with the (projection) point $\mathbf{p}_1$; see Figure 2.1. The projection ray can be expressed in the optical coordinate system which has its origin at $\mathbf{C}_1$; in this case it is written as $\mathcal{L}_{\mathbf{c}_1}$ for distinction from other representations. (Ray $\mathcal{L}$ may also be expressed in another coordinate system in a context
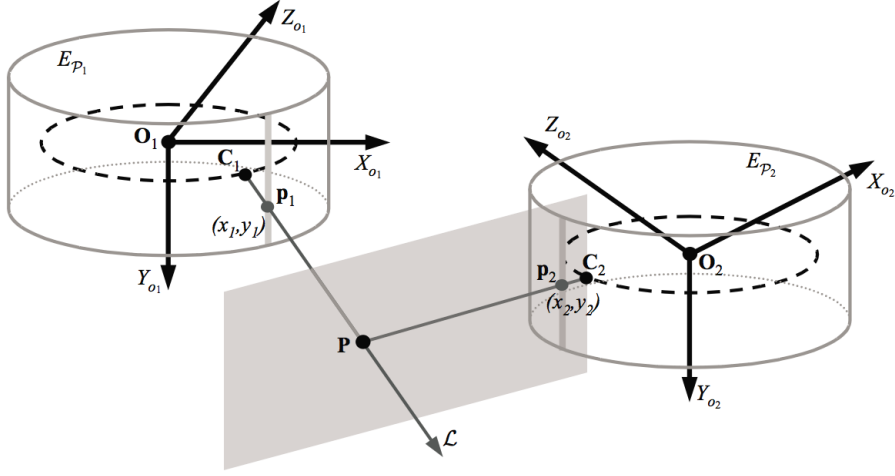
Figure 2.1.   Pair of cylindric panoramas in general position and orientation.

as specified below.) The projection ray $\mathcal{L}_{\mathbf{c}_1}$ can be described by $\mathbf{0} + \lambda\mathbf{D}$, where $\mathbf{0}$ is a 3D zero vector, $\lambda \in \Re$ is any scalar, and $\mathbf{D}$ is a directional unit vector defined as follows:

$$\mathbf{D} = \begin{bmatrix} 0 \\ \sin\arctan(\frac{y_1}{f_1}) \\ \cos\arctan(\frac{y_1}{f_1}) \end{bmatrix} = \begin{bmatrix} 0 \\ \sin\beta_1 \\ \cos\beta_1 \end{bmatrix} \tag{1}$$

The projection ray $\mathcal{L}_{\mathbf{c}_1}$ is then transformed into the camera coordinate system (with origin at $\mathbf{O}_1$) of the source panoramic image $E_{\mathcal{P}_1}$, denoted as $\mathcal{L}_{\mathbf{o}_1}$. We have

$$\begin{aligned} \mathcal{L}_{\mathbf{o}_1} &= \begin{bmatrix} \mathbf{R}_{\mathbf{o}_1\mathbf{c}_1}^{-1} & \mathbf{T}_{\mathbf{o}_1\mathbf{c}_1} \end{bmatrix} \begin{bmatrix} \mathcal{L}_{\mathbf{c}_1} \\ 1 \end{bmatrix} \\ &= \begin{bmatrix} \mathbf{R}_{\mathbf{o}_1\mathbf{c}_1}^{-1} & \mathbf{T}_{\mathbf{o}_1\mathbf{c}_1} \end{bmatrix} \begin{bmatrix} \mathbf{0} + \lambda\mathbf{D} \\ 1 \end{bmatrix} \\ &= \mathbf{T}_{\mathbf{o}_1\mathbf{c}_1} + \lambda\mathbf{R}_{\mathbf{o}_1\mathbf{c}_1}^{-1}\mathbf{D} \end{aligned} \tag{2}$$

where rotation matrix $\mathbf{R}_{\mathbf{o}_1\mathbf{c}_1}$ or translation vector $\mathbf{T}_{\mathbf{o}_1\mathbf{c}_1}$ specify orientation or position of the optical coordinate system (with origin at $\mathbf{C}_1$) with respect to the camera coordinate system (with origin at $\mathbf{O}_1$), respectively.

To calculate the potential positions of the corresponding point of $\mathbf{p}_1$ in the destination panorama, a further transform of the projection ray $\mathcal{L}_{\mathbf{o}_1}$ is necessary into the panorama coordinate system (with origin at $\mathbf{O}_2$) of the destination panoramic image $E_{\mathcal{P}_2}$. The transformed projection ray is

denoted as $\mathcal{L}_{\mathbf{o}_2}$. We have the following:

$$
\begin{aligned}
\mathcal{L}_{\mathbf{o}_2} &= [\mathbf{R}_{\mathbf{o}_1\mathbf{o}_2} \ -\mathbf{R}_{\mathbf{o}_1\mathbf{o}_2}\mathbf{T}_{\mathbf{o}_1\mathbf{o}_2}] \begin{bmatrix} \mathcal{L}_{\mathbf{o}_1} \\ 1 \end{bmatrix} \\
&= [\mathbf{R}_{\mathbf{o}_1\mathbf{o}_2} \ -\mathbf{R}_{\mathbf{o}_1\mathbf{o}_2}\mathbf{T}_{\mathbf{o}_1\mathbf{o}_2}] \begin{bmatrix} \mathbf{T}_{\mathbf{o}_1\mathbf{c}_1} + \lambda\mathbf{R}_{\mathbf{o}_1\mathbf{c}_1}^{-1}\mathbf{D} \\ 1 \end{bmatrix} \\
&= \mathbf{R}_{\mathbf{o}_1\mathbf{o}_2}\mathbf{T}_{\mathbf{o}_1\mathbf{c}_1} + \lambda\mathbf{R}_{\mathbf{o}_1\mathbf{o}_2}\mathbf{R}_{\mathbf{o}_1\mathbf{c}_1}^{-1}\mathbf{D} - \mathbf{R}_{\mathbf{o}_1\mathbf{o}_2}\mathbf{T}_{\mathbf{o}_1\mathbf{o}_2} \\
&= \mathbf{R}_{\mathbf{o}_1\mathbf{o}_2}\left(\mathbf{T}_{\mathbf{o}_1\mathbf{c}_1} - \mathbf{T}_{\mathbf{o}_1\mathbf{o}_2} + \lambda\mathbf{R}_{\mathbf{o}_1\mathbf{c}_1}^{-1}\mathbf{D}\right) \qquad (3)
\end{aligned}
$$

where rotation matrix $\mathbf{R}_{\mathbf{o}_1\mathbf{o}_2}$ or translation vector $\mathbf{T}_{\mathbf{o}_1\mathbf{o}_2}$ specify orientation or position of the camera coordinate system (with origin at $\mathbf{O}_2$) or with respect to the camera coordinate system (with origin at $\mathbf{O}_1$), respectively.

We expand the rotation matrix $\mathbf{R}_{\mathbf{o}_1\mathbf{c}_1}$ and the translation vector $\mathbf{T}_{\mathbf{o}_1\mathbf{c}_1}$ in Equation (3), and substitute the unit vector $\mathbf{D}$ as given in Equation (1). The equation of the projection ray $\mathcal{L}_{\mathbf{o}_2}$ is thus as follows:

$$
\begin{aligned}
\mathcal{L}_{\mathbf{o}_2} &= \mathbf{R}_{\mathbf{o}_1\mathbf{o}_2}\left(\begin{bmatrix} R_1\sin\alpha_1 \\ 0 \\ R_1\cos\alpha_1 \end{bmatrix} - \mathbf{T}_{\mathbf{o}_1\mathbf{o}_2} + \lambda \begin{bmatrix} \cos(\alpha_1+\omega_1) & 0 & \sin(\alpha_1+\omega_1) \\ 0 & 1 & 0 \\ -\sin(\alpha_1+\omega_1) & 0 & \cos(\alpha_1+\omega_1) \end{bmatrix} \begin{bmatrix} 0 \\ \sin\beta_1 \\ \cos\beta_1 \end{bmatrix}\right) \\
&= \mathbf{R}_{\mathbf{o}_1\mathbf{o}_2}\left(\begin{bmatrix} R_1\sin\alpha_1 \\ 0 \\ R_1\cos\alpha_1 \end{bmatrix} - \mathbf{T}_{\mathbf{o}_1\mathbf{o}_2} + \lambda \begin{bmatrix} \sin\delta_1\cos\beta_1 \\ \sin\beta_1 \\ \cos\delta_1\cos\beta_1 \end{bmatrix}\right) \qquad (4)
\end{aligned}
$$

where R_1 and ω_1 are the camera off-axis distance and principal angle of the source panorama, respectively, and α_1 and β_1 are the angular image coordinates of image point (x_1, y_1). We have $\delta_1 = (\alpha_1 + \omega_1)$.

Furthermore, in the theorem the rotation matrix $\mathbf{R}_{\mathbf{o}_1\mathbf{o}_2}$ is decomposed into its three row vectors as $[\mathbf{r}_1^T\mathbf{r}_2^T\mathbf{r}_3^T]^T$, and the translation vector is represented by three elements as $(t_x, t_y, t_z)^T$. The presentation of the projection ray $\mathcal{L}_{\mathbf{o}_2}$ in Equation (4) is rearranged as follows:

$$
\begin{aligned}
\mathcal{L}_{\mathbf{o}_2} &= \begin{bmatrix} \mathbf{r}_1^T \\ \mathbf{r}_2^T \\ \mathbf{r}_3^T \end{bmatrix}\left(\begin{bmatrix} R_1\sin\alpha_1 \\ 0 \\ R_1\cos\alpha_1 \end{bmatrix} - \begin{bmatrix} t_x \\ t_y \\ t_z \end{bmatrix} + \lambda \begin{bmatrix} \sin\delta_1\cos\beta_1 \\ \sin\beta_1 \\ \cos\delta_1\cos\beta_1 \end{bmatrix}\right) \\
&= \mathbf{R}_{\mathbf{o}_1\mathbf{o}_2}\left(\mathbf{A} + \lambda\mathbf{B}\right) \\
&= \begin{bmatrix} \mathbf{r}_1^T{\cdot}\mathbf{A} + \lambda\mathbf{r}_1^T{\cdot}\mathbf{B} \\ \mathbf{r}_2^T{\cdot}\mathbf{A} + \lambda\mathbf{r}_2^T{\cdot}\mathbf{B} \\ \mathbf{r}_3^T{\cdot}\mathbf{A} + \lambda\mathbf{r}_3^T{\cdot}\mathbf{B} \end{bmatrix} \qquad (5)
\end{aligned}
$$

where $\lambda \in \Re$ is any scalar, and vectors $\mathbf{A}$ and $\mathbf{B}$ are specified in the theorem.

Let point $\mathbf{p}_2$ denote the corresponding point of $\mathbf{p}_1$ in the destination image $E_{\mathcal{P}_2}$. Point $\mathbf{p}_2$ is the projection of some (unknown) 3D point on ray

$\mathcal{L}_{\mathbf{o}_2}$. The epipolar curve equation describes the projection of ray $\mathcal{L}_{\mathbf{o}_2}$ onto image $E_{\mathcal{P}_2}$, and is thus an equation in x_2 and y_2.

Let $\mathbf{C}_2$ denote the optical point associated with image column x_2 of $E_{\mathcal{P}_2}$. For each column x_2, the corresponding y_2 value can be found by the following two steps. First, find the intersection point, denoted as $\mathbf{P}$, of ray $\mathcal{L}_{\mathbf{o}_2}$ with t he plane $\wp$ which is incident with $\mathbf{C}_2$ and image column x_2. Second, obtain y_2 by projecting point $\mathbf{P}$ into the image column x_2 of panorama $E_{\mathcal{P}_2}$ (see Figure 2.1).

The equation of plane $\wp$ is as follows,

$$-\cos(\alpha_2 + \omega_2)X + \sin(\alpha_2 + \omega_2)Z = R_2 \sin \omega_2 \tag{6}$$

where R_2 or ω_2 are camera off-axis distance or principal angle of the destination panorama, respectively, and α_2 is the angular image coordinate of image point $\mathbf{p}_2$.

We substitute the X- and Z-coordinates of projection ray $\mathcal{L}_{\mathbf{o}_2}$ in Equation (5) into Equation (6) and solve it for λ. We obtain the following:

$$-\cos(\alpha_2 + \omega_2)(\mathbf{r}_1^{\mathrm{T}} \cdot \mathbf{A} + \lambda \mathbf{r}_1^{\mathrm{T}} \cdot \mathbf{B}) + \sin(\alpha_2 + \omega_2)(\mathbf{r}_3^{\mathrm{T}} \cdot \mathbf{A} + \lambda \mathbf{r}_3^{\mathrm{T}} \cdot \mathbf{B}) = R_2 \sin \omega_2$$

and thus

$$\lambda = \frac{R_2 \sin \omega_2 + \cos(\alpha_2 + \omega_2)\mathbf{r}_1^{\mathrm{T}} \cdot \mathbf{A} - \sin(\alpha_2 + \omega_2)\mathbf{r}_3^{\mathrm{T}} \cdot \mathbf{A}}{\sin(\alpha_2 + \omega_2)\mathbf{r}_3^{\mathrm{T}} \cdot \mathbf{B} - \cos(\alpha_2 + \omega_2)\mathbf{r}_1^{\mathrm{T}} \cdot \mathbf{B}}$$

We define $\mathbf{V} = \mathbf{A} + \lambda \mathbf{B}$ (note: as in the theorem).

The intersection point $\mathbf{P}$ can now be calculated by substituting λ into Equation (5). We denote the obtained coordinates of $\mathbf{P}$ as $(X_{o_2}, Y_{o_2}, Z_{o_2})^{\mathrm{T}}$ with respect to the camera coordinate system (with origin at $\mathbf{O}_2$). We have

$$
\begin{aligned}
\begin{bmatrix} X_{o_2} \\ Y_{o_2} \\ Z_{o_2} \end{bmatrix} &= \mathbf{R}_{\mathbf{o}_1\mathbf{o}_2}(\mathbf{A} + \lambda \mathbf{B}) \\
&= \mathbf{R}_{\mathbf{o}_1\mathbf{o}_2}\mathbf{V} \\
&= \begin{bmatrix} \mathbf{r}_1^{\mathrm{T}} \cdot \mathbf{V} \\ \mathbf{r}_2^{\mathrm{T}} \cdot \mathbf{V} \\ \mathbf{r}_3^{\mathrm{T}} \cdot \mathbf{V} \end{bmatrix}
\end{aligned}
\tag{7}
$$

The point $\mathbf{P}$ is transformed into the optical coordinate system (with origin at $\mathbf{C}_2$) for calculating the projection of the image. We denote the coordinates of $\mathbf{P}$ after transformation as $(X_{c_2}, Y_{c_2}, Z_{c_2})^{\mathrm{T}}$. We have the following:

$$
\begin{bmatrix} X_{c_2} \\ Y_{c_2} \\ Z_{c_2} \end{bmatrix} = [\mathbf{R}_{\mathbf{o}_2\mathbf{c}_2} \quad -\mathbf{R}_{\mathbf{o}_2\mathbf{c}_2}\mathbf{T}_{\mathbf{o}_2\mathbf{c}_2}] \begin{bmatrix} X_{o_2} \\ Y_{o_2} \\ Z_{o_2} \\ 1 \end{bmatrix}
$$

where rotation matrix $\mathbf{R_{o_2c_2}}$ or translation vector $\mathbf{T_{o_2c_2}}$ specify orientation or position of the optical coordinate system (with origin at $\mathbf{C}_2$) with respect to the camera coordinate system (with origin at $\mathbf{O}_2$), respectively. After expansion we obtain the following:

$$
\begin{bmatrix} X_{c_2} \\ Y_{c_2} \\ Z_{c_2} \end{bmatrix} = \begin{bmatrix} \cos(\alpha_2+\omega_2) & 0 & -\sin(\alpha_2+\omega_2) \\ 0 & 1 & 0 \\ \sin(\alpha_2+\omega_2) & 0 & \cos(\alpha_2+\omega_2) \end{bmatrix} \begin{bmatrix} X_{o_2} - R_2\sin\alpha_2 \\ Y_{o_2} \\ Z_{o_2} - R_2\cos\alpha_2 \end{bmatrix}
$$

$$
= \begin{bmatrix} (X_{o_2}-R_2\sin\alpha_2)\cos(\alpha_2+\omega_2)-(Z_{o_2}-R_2\cos\alpha_2)\sin(\alpha_2+\omega_2) \\ Y_{o_2} \\ (X_{o_2}-R_2\sin\alpha_2)\sin(\alpha_2+\omega_2)+(Z_{o_2}-R_2\cos\alpha_2)\cos(\alpha_2+\omega_2) \end{bmatrix}
$$

$$
= \begin{bmatrix} X_{o_2}\cos(\alpha_2+\omega_2)-Z_{o_2}\sin(\alpha_2+\omega_2)+R_2\sin\omega_2 \\ Y_{o_2} \\ X_{o_2}\sin(\alpha_2+\omega_2)+Z_{o_2}\cos(\alpha_2+\omega_2)-R_2\cos\omega_2 \end{bmatrix}
$$

Note that the value of X_{c_2} is equal to zero (as expected). We omit more details here of further derivations because they are all straightforward formula transformations.

To obtain the value of y_2, the point $(X_{c_2}, Y_{c_2}, Z_{c_2})^{\mathrm{T}}$ is projected into image column x_2 by the following projection formula:

$$
y_2 = \frac{f_2 Y_{c_2}}{Z_{c_2}} \tag{8}
$$

$$
= \frac{f_2 Y_{o_2}}{X_{o_2}\sin(\alpha_2+\omega_2)+Z_{o_2}\cos(\alpha_2+\omega_2)-R_2\cos\omega_2}
$$

where X_{o_2}, Y_{o_2}, and Z_{o_2} can be substituted following Equation (7). Thus we obtain the following epipolar curve equation (as stated in the theorem):

$$
y_2 = \frac{f_2 \mathbf{r}_2^{\mathrm{T}} \cdot \mathbf{V}}{\mathbf{r}_1^{\mathrm{T}} \cdot \mathbf{V}\sin(\alpha_2+\omega_2)+\mathbf{r}_3^{\mathrm{T}} \cdot \mathbf{V}\cos(\alpha_2+\omega_2)-R_2\cos\omega_2} \tag{9}
$$

Finally, according to the projection formula in Equation (8), in cases where the value of Z_{c_2} is equal to zero (less than zero), the value of y_2 remains undefined (is of opposite sign to the value of Y_{c_2}). In both cases, the resulting projection (x_2, y_2) of the 3D point $(X_{c_2}, Y_{c_2}, Z_{c_2})^{\mathrm{T}}$ is invalid. Therefore, Equation (9) is only valid if the Z_c-coordinate of the 3D point is greater than zero (i.e., the denominator of y_2 needs to be greater than zero). $\square$

The general epipolar curve equation stated in Theorem 2.1 for an arbitrary pair of cylindric panoramas is rather 'complicated and lengthy'. It is difficult to imagine the geometry of epipolar curves by reading the equation. However, this equation is useful for further mathematical analysis (as
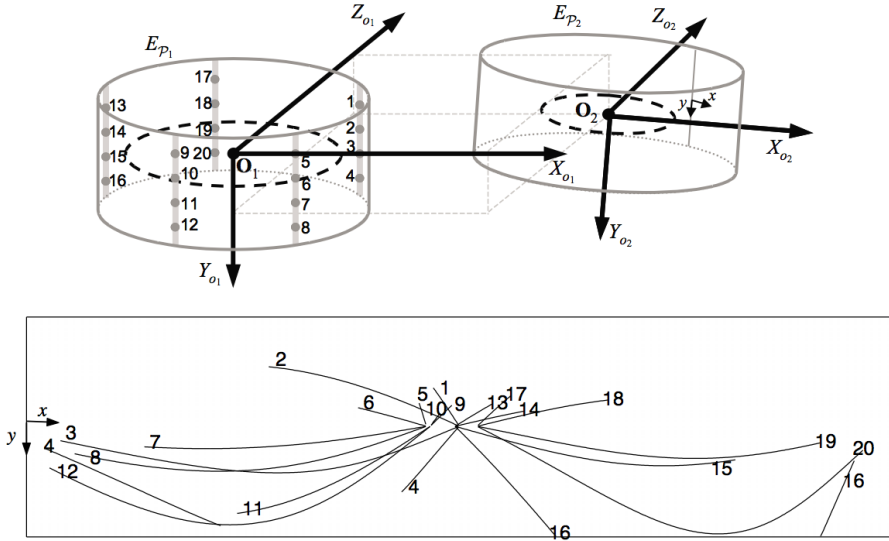
Figure 2.2. A pair of polycentric panoramas and epipolar curves in the destination image originating from 20 selected points in the source image $E_{\mathcal{P}_1}$.

shown below), and characterizes epipolar geometry for any pair of cylindric panoramas.

Example 1. Figure 2.2 illustrates an example of epipolar curves for a general case of a pair of panoramic images. The shown curves demonstrate the geometric complexity of those curves.

The internal camera parameters of source panorama $E_{\mathcal{P}_1}(R_1, f, \omega_1, \gamma)$ and destination panorama $E_{\mathcal{P}_2}(R_2, f, \omega_2, \gamma)$ are as follows: $R_1 = 500mm$, $\omega_1 = 45°$, $R_2 = 250mm$, $\omega_2 = 65°$, $f = 35mm$, and $\gamma = 0.36°$.

The affine transform between both camera coordinate systems (associated with these two panoramas) can be described by a translation vector $\mathbf{T_{o_1o_2}}$ and a rotation matrix $\mathbf{R_{o_1o_2}}$. We set $\mathbf{T_{o_1o_2}} = (2000, 300, 1500)^{\mathrm{T}}$ in mm and $\mathbf{R_{o_1o_2}} = \mathbf{R}_x(-1°)\mathbf{R}_y(-1°)\mathbf{R}_z(2°)$, where $\mathbf{R}_x$, $\mathbf{R}_y$, and $\mathbf{R}_z$ are rotation matrixes with respect to each of the three axes. The top of Figure 2.2 shows the specified geometric relation between these two panoramas in 3D space.

20 points have been selected in image $E_{\mathcal{P}_1}$, labeled by numbers. The corresponding epipolar curves in image $E_{\mathcal{P}_2}$, also labeled by numbers, are shown at the bottom of Figure 2.2. An interesting observation is that epipolar curves do cross each other (in this case), and these intersections are not necessarily epipoles (for example, curves 3 and 8). This is a new situation compared to epipolar geometry of pinhole cameras where epipolar

lines only intersect at epipoles. However, if we only consider epipolar curves associated with image points on the same column of the source image $E_{\mathcal{P}_1}$, for example curves labeled 17,18,19 and 20, then they only intersect (if at all) at epipoles.

Traditionally panoramas are assumed to be single centered (i.e., single projection center), that means the off-axis distance R is equal to zero. This is a special case of our general camera model, and we illustrate it in the next example.

Example 2. All the internal camera parameters and the affine transform between both panoramas remain the same as in Example 1, except that we take $R_1 = R_2 = 0$. Resulting epipolar curves are shown in Figure 2.3. In this case, all epipolar curves intersect exactly at one point (i.e., the epipole).
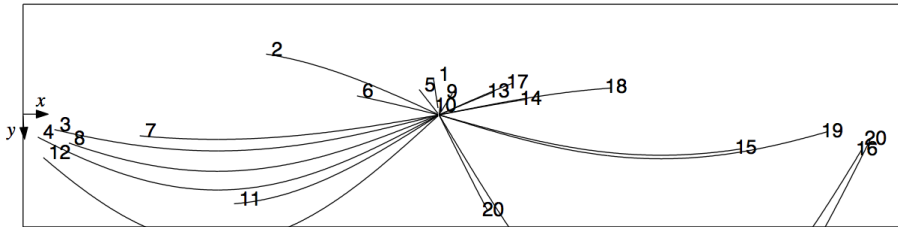

Figure 2.3. Epipolar curves for the single-center (i.e., $R=0$) case of Example 2.

The epipolar geometry of cylindric single-center panoramas has been discussed in (McMillan and Bishop, 1995a; Kang and Szeliski, 1997; Shum et al., 1998). In these approaches, each of the single-center panoramas is composed by stitching of planar (i.e., pinhole) images. Negative results in stereo matching are linked in these cases to inaccurate epipolar geometry estimation. However, practical experiments show that a cylindric panorama produced by rotating a camera (e.g., on a tripod) is rarely satisfying the single-center assumption $R = 0$, not to mention the case of stitched images. Thus, negative results in stereo matching are totally foreseeable if using an ideal (oversimplified) single-center camera model to estimate the epipolar geometry in such cases.

The polycentric case should be used instead. Differences between cases shown in Figure 2.2(bottom) and Figure 2.3 illustrate the importance of the general model. As a consequence, it is necessary to calibrate and model the off-axis distance R, and (in general) also the principal angle ω for any stereo application that uses cylindric panoramas.

2.2. Constrained Poses of Cameras

The general epipolar curve equation of Theorem 2.1 is not a polynomial, 'lengthy', and 'complicated' due to the geometric complexity of the general cylindric panoramic camera model. As a result, the estimation of the epipolar geometry from corresponding points of a polycentric panoramic pair may suffer severe numerical instability. This problem motivates us to constrain relative poses of panoramic cameras to some particular cases for practical purposes (e.g., to ensure computational simplicity, or numeric stability).

This section discusses a few cases of constrained poses of panoramic pairs, where each case has its own practical merits and also existing applications. The selected cases include leveled, co-axis, concentric, and symmetric panoramic pairs. We illustrate how Theorem 2.1 can be regarded as general guidance for computing epipolar curves for the whole family of cylindric panoramas.

This section is organized in an order by going from general to more specific cases. We first elaborate the derivation of the epipolar curve equation for a leveled panoramic pair, and the remaining cases then benefit from this derived epipolar curve equation.

2.2.1. LEVELED PANORAMIC PAIR

In many applications, multiple panoramic images acquired at different viewpoints are necessary, for example, for 3D reconstructions of large historical sites or big shopping mall interiors, or for creating virtual tours of museums or of famous scenic places. Epipolar geometry serves as a fundamental tool in various processes of those applications, such as image correspondence analysis, relative pose estimation, or novel view synthesis, where epipolar curves may be used to determine traversal paths or orders of image points.

An intuitive and practical way to reduce the dimensionality of the general epipolar curve equation is to make all associated base planes of panoramas leveled with the sea level (e.g., by cameras on leveled tripods using a "bull's eye" or more advanced leveling devices). In the model chapter, a polycentric panoramic pair whose associated axes are orthogonal to sea level was called a leveled panoramic pair.

Note that the elevations of cameras contributing to a leveled panoramic pair can be different. Under the assumption that a panoramic pair is perfectly leveled, the general epipolar curve equation in Theorem 2.1 can be simplified.

COROLLARY 2.1. *Let (x_1, y_1) and (x_2, y_2) be a pair of corresponding image points in a pair of leveled polycentric panoramas $E_{\mathcal{P}_1}(R_1, f_1, \omega_1, \gamma)$*

and $E_{\mathcal{P}_2}(R_2, f_2, \omega_2, \gamma)$, respectively. Given x_1 and y_1, the epipolar curve equation in this case is as follows:

$$y_2 = \frac{y_1\left(\frac{f_2}{f_1}\right)(R_2\sin\omega_2 - R_1\sin(\sigma_2-\alpha_1) - t_x\cos\sigma_2 + t_z\sin\sigma_2) - t_y f_2\sin(\sigma_2-\sigma_1)}{R_2\sin(\sigma_1-\alpha_2-\phi) - R_1\sin\omega_1 - t_x\cos\sigma_1 + t_z\sin\sigma_1}$$

where $\alpha_1 = \frac{2\pi x_1}{\mu W_1}$, $\alpha_2 = \frac{2\pi x_2}{\mu W_2}$, $\sigma_1 = (\alpha_1 + \omega_1)$, and $\sigma_2 = (\alpha_2 + \omega_2 + \phi)$, and the angle ϕ determines the rotation with respect to the y-axis.

Proof We derive this equation from the general epipolar curve equation in Theorem 2.1. The meanings of notations used in the proof are as in the proof of Theorem 2.1.

In the leveled case, the 3×3 rotation matrix (that specifies the orientation of the camera coordinate system of the destination image with respect to the camera coordinate system of the source image) only consists of one variable that describes the rotation with respect to the Y-axis. We describe this rotation by angle ϕ. The three row vectors of the rotation matrix become $\mathbf{r}_1^{\mathrm{T}} = (\cos\phi, 0, -\sin\phi)^{\mathrm{T}}$, $\mathbf{r}_2^{\mathrm{T}} = (0, 1, 0)^{\mathrm{T}}$, and $\mathbf{r}_3^{\mathrm{T}} = (\sin\phi, 0, \cos\phi)^{\mathrm{T}}$.

Step by step, we substitute these row vectors of the rotation matrix into the general epipolar curve equation of Theorem 2.1. First, we calculate $\mathbf{r}_1^{\mathrm{T}}\cdot\mathbf{A}$, $\mathbf{r}_3^{\mathrm{T}}\cdot\mathbf{A}$, $\mathbf{r}_1^{\mathrm{T}}\cdot\mathbf{B}$, and $\mathbf{r}_3^{\mathrm{T}}\cdot\mathbf{B}$. It follows that

$$\begin{aligned}
\mathbf{r}_1^{\mathrm{T}}\cdot\mathbf{A} &= [\cos\phi, 0, -\sin\phi]^{\mathrm{T}}\begin{bmatrix} R_1\sin\alpha_1 - t_x \\ -t_y \\ R_1\cos\alpha_1 - t_z \end{bmatrix} \\
&= R_1\sin\alpha_1\cos\phi - t_x\cos\phi - R_1\cos\alpha_1\sin\phi + t_z\sin\phi \\
&= R_1\sin(\alpha_1 - \phi) - t_x\cos\phi + t_z\sin\phi
\end{aligned}$$

$$\begin{aligned}
\mathbf{r}_3^{\mathrm{T}}\cdot\mathbf{A} &= [\sin\phi, 0, \cos\phi]^{\mathrm{T}}\begin{bmatrix} R_1\sin\alpha_1 - t_x \\ -t_y \\ R_1\cos\alpha_1 - t_z \end{bmatrix} \\
&= R_1\sin\alpha_1\sin\phi - t_x\sin\phi + R_1\cos\alpha_1\sin\phi - t_z\cos\phi \\
&= R_1\cos(\alpha_1 - \phi) - t_x\sin\phi - t_z\cos\phi
\end{aligned}$$

$$\begin{aligned}
\mathbf{r}_1^{\mathrm{T}}\cdot\mathbf{B} &= [\cos\phi, 0, -\sin\phi]^{\mathrm{T}}\begin{bmatrix} \sin(\alpha_1+\omega_1)\cos\beta_1 \\ \sin\beta_1 \\ \cos(\alpha_1+\omega_1)\cos\beta_1 \end{bmatrix} \\
&= \sin(\alpha_1+\omega_1)\cos\beta_1\cos\phi - \cos(\alpha_1+\omega_1)\cos\beta_1\sin\phi \\
&= \cos\beta_1\sin(\alpha_1+\omega_1-\phi)
\end{aligned}$$

$$\mathbf{r}_3^{\mathrm{T}} \cdot \mathbf{B} = [\sin\phi, 0, \cos\phi]^{\mathrm{T}} \begin{bmatrix} \sin(\alpha_1 + \omega_1)\cos\beta_1 \\ \sin\beta_1 \\ \cos(\alpha_1 + \omega_1)\cos\beta_1 \end{bmatrix}$$

$$= \sin(\alpha_1 + \omega_1)\cos\beta_1 \sin\phi + \cos(\alpha_1 + \omega_1)\cos\beta_1 \cos\phi$$

$$= \cos\beta_1 \cos(\alpha_1 + \omega_1 - \phi)$$

In order to calculate vector $\mathbf{V}$ in Theorem 2.1, we first calculate the following two partial terms of vector $\mathbf{V}$. Firstly,

$$\cos(\alpha_2 + \omega_2)\mathbf{r}_1^{\mathrm{T}} \cdot \mathbf{A} - \sin(\alpha_2 + \omega_2)\mathbf{r}_3^{\mathrm{T}} \cdot \mathbf{A}$$

$$= R_1 \sin(\alpha_1 - \phi)\cos(\alpha_2 + \omega_2) - t_x \cos\phi \cos(\alpha_2 + \omega_2) + t_z \sin\phi \cos(\alpha_2 + \omega_2)$$

$$\quad - R_1 \cos(\alpha_1 - \phi)\sin(\alpha_2 + \omega_2) + t_x \sin\phi \sin(\alpha_2 + \omega_2) + t_z \cos\phi \sin(\alpha_2 + \omega_2)$$

$$= R_1 \sin(\alpha_1 - \phi - \alpha_2 - \omega_2) - t_x \cos(\phi + \alpha_2 + \omega_2) + t_z \sin(\phi + \alpha_2 + \omega_2)$$

and secondly,

$$\sin(\alpha_2 + \omega_2)\mathbf{r}_3^{\mathrm{T}} \cdot \mathbf{B} - \cos(\alpha_2 + \omega_2)\mathbf{r}_1^{\mathrm{T}} \cdot \mathbf{B}$$

$$= \cos\beta_1 \sin(\alpha_2 + \omega_2)\cos(\alpha_1 + \omega_1 - \phi) - \cos\beta_1 \cos(\alpha_2 + \omega_2)\sin(\alpha_1 + \omega_1 - \phi)$$

$$= \cos\beta_1 \sin(\alpha_2 + \omega_2 - \alpha_1 - \omega_1 + \phi)$$

To simplify the equations, let $\sigma_1 = (\alpha_1 + \omega_1)$ and $\sigma_2 = (\alpha_2 + \omega_2 + \phi)$. Vector $\mathbf{V}$ is as defined in Theorem 2.1, and it is equal to

$$\mathbf{A} + \frac{R_2 \sin\omega_2 + R_1 \sin(\alpha_1 - \sigma_2) - t_x \cos\sigma_2 + t_z \sin\sigma_2}{\cos\beta_1 \sin(\sigma_2 - \sigma_1)} \mathbf{B}$$

$$= \begin{bmatrix} R_1 \sin\alpha_1 - t_x \\ -t_y \\ R_1 \cos\alpha_1 - t_z \end{bmatrix} + \frac{R_2 \sin\omega_2 + R_1 \sin(\alpha_1 - \sigma_2) - t_x \cos\sigma_2 + t_z \sin\sigma_2}{\sin(\sigma_2 - \sigma_1)} \begin{bmatrix} \sin\sigma_1 \\ \tan\beta_1 \\ \cos\sigma_1 \end{bmatrix}$$

Let $\mathbf{V} = \frac{1}{\sin(\sigma_2 - \sigma_1)}(v_x, v_y, v_z)^{\mathrm{T}}$. We have

$$v_x = R_1 \sin\alpha_1 \sin(\sigma_2 - \sigma_1) - t_x \sin(\sigma_2 - \sigma_1) + R_2 \sin\omega_2 \sin\sigma_1$$

$$\quad + R_1 \sin(\alpha_1 - \sigma_2)\sin\sigma_1 - t_x \cos\sigma_2 \sin\sigma_1 + t_z \sin\sigma_2 \sin\sigma_1$$

$$v_y = \tan\beta_1 (R_2 \sin\omega_2 + R_1 \sin(\alpha_1 - \sigma_2) - t_x \cos\sigma_2 + t_z \sin\sigma_2) - t_y \sin(\sigma_2 - \sigma_1)$$

$$v_z = R_1 \cos\alpha_1 \sin(\sigma_2 - \sigma_1) - t_z \sin(\sigma_2 - \sigma_1) + R_2 \sin\omega_2 \cos\sigma_1$$

$$\quad + R_1 \sin(\alpha_1 - \sigma_2)\cos\sigma_1 - t_x \cos\sigma_2 \cos\sigma_1 + t_z \sin\sigma_2 \cos\sigma_1$$

The numerator of y_2 in Theorem 2.1 becomes

$$f_2 \mathbf{r}_2^{\mathrm{T}} \cdot \mathbf{V}$$

$$= \frac{f_2}{\sin(\sigma_2 - \sigma_1)} (0, 1, 0) \begin{bmatrix} v_x \\ v_y \\ v_z \end{bmatrix}$$

$$= \frac{f_2 v_y}{\sin(\sigma_2 - \sigma_1)}$$

$$= \frac{y_1 \left(\frac{f_2}{f_1}\right) (R_2 \sin\omega_2 + R_1 \sin(\alpha_1 - \sigma_2) - t_x \cos\sigma_2 + t_z \sin\sigma_2) - t_y f_2 \sin(\sigma_2 - \sigma_1)}{\sin(\sigma_2 - \sigma_1)}$$

Note that we have $\tan\beta_1 = \frac{y_1}{f_1}$ in the equation for v_y, which eliminates the need to use the tan function. Furthermore, the denominator of y_2 in Theorem 2.1 becomes

$$\sin\delta_2 \mathbf{r}_1^{\mathrm{T}} \cdot \mathbf{V} + \cos\delta_2 \mathbf{r}_3^{\mathrm{T}} \cdot \mathbf{V} - R_2 \cos\omega_2$$

$$= \frac{\sin(\alpha_2 + \omega_2)}{\sin(\sigma_2 - \sigma_1)}[\cos\phi, 0, -\sin\phi]^{\mathrm{T}} \begin{bmatrix} v_x \\ v_y \\ v_z \end{bmatrix}$$

$$+ \frac{\cos(\alpha_2 + \omega_2)}{\sin(\sigma_2 - \sigma_1)}[\sin\phi, 0, \cos\phi]^{\mathrm{T}} \begin{bmatrix} v_x \\ v_y \\ v_z \end{bmatrix} - R_2 \cos\omega_2$$

$$= \frac{v_x \sin(\alpha_2 + \omega_2)\cos\phi - v_z \sin(\alpha_2 + \omega_2)\sin\phi}{\sin(\sigma_2 - \sigma_1)}$$

$$+ \frac{v_x \cos(\alpha_2 + \omega_2)\sin\phi + v_z \cos(\alpha_2 + \omega_2)\cos\phi}{\sin(\sigma_2 - \sigma_1)} - R_2 \cos\omega_2$$

$$= \frac{1}{\sin(\sigma_2 - \sigma_1)} \left(v_x \sin(\alpha_2 + \omega_2 + \phi) + v_z \cos(\alpha_2 + \omega_2 + \phi)\right) - R_2 \cos\omega_2$$

$$= \frac{1}{\sin(\sigma_2 - \sigma_1)} \left(R_1 \sin\alpha_1 \sin\sigma_2 \sin(\sigma_2 - \sigma_1) - t_x \sin\sigma_2 \sin(\sigma_2 - \sigma_1)\right.$$
$$+ R_2 \sin\omega_2 \sin\sigma_2 \sin\sigma_1 + R_1 \sin\sigma_2 \sin(\alpha_1 - \sigma_2)\sin\sigma_1 - t_x \sin\sigma_2 \cos\sigma_2 \sin\sigma_1$$
$$+ t_z \sin^2\sigma_2 \sin\sigma_1 + R_1 \cos\alpha_1 \cos\sigma_2 \sin(\sigma_2 - \sigma_1) - t_z \cos\sigma_2 \sin(\sigma_2 - \sigma_1)$$
$$+ R_2 \sin\omega_2 \cos\sigma_2 \cos\sigma_1 + R_1 \cos\sigma_2 \sin(\alpha_1 - \sigma_2)\cos\sigma_1 - t_x \cos^2\sigma_2 \cos\sigma_1$$
$$\left.+ t_z \sin\sigma_2 \cos\sigma_2 \cos\sigma_1 - R_2 \cos\omega_2 \sin(\sigma_2 - \sigma_1)\right)$$

$$= \frac{1}{\sin(\sigma_2 - \sigma_1)} \left(R_1 \cos(\alpha_1 - \sigma_2)\sin(\sigma_2 - \sigma_1) - t_x \sin\sigma_2 \sin(\sigma_2 - \sigma_1)\right.$$
$$- t_z \cos\sigma_2 \sin(\sigma_2 - \sigma_1) + R_2 \sin\omega_2 \cos(\sigma_2 - \sigma_1) + R_1 \sin(\alpha_1 - \sigma_2)\cos(\sigma_2 - \sigma_1)$$
$$\left.- t_x \cos\sigma_2 \cos(\sigma_2 - \sigma_1) + t_z \sin\sigma_2 \cos(\sigma_2 - \sigma_1) - R_2 \cos\omega_2 \sin(\sigma_2 - \sigma_1)\right)$$

$$= \frac{1}{\sin(\sigma_2 - \sigma_1)} \left(R_1 \sin(\alpha_1 - \sigma_1) - t_x \cos\sigma_1 + t_z \sin\sigma_1 + R_2 \sin(\omega_2 - \sigma_2 + \sigma_1)\right)$$

Thus we have that the value of y_2 is as follows:

$$y_2 = \frac{y_1 \left(\frac{f_2}{f_1}\right)(R_2 \sin\omega_2 - R_1 \sin(\sigma_2 - \alpha_1) - t_x \cos\sigma_2 + t_z \sin\sigma_2) - t_y f_2 \sin(\sigma_2 - \sigma_1)}{R_2 \sin(\sigma_1 - \alpha_2 - \phi) - R_1 \sin\omega_1 - t_x \cos\sigma_1 + t_z \sin\sigma_1}$$
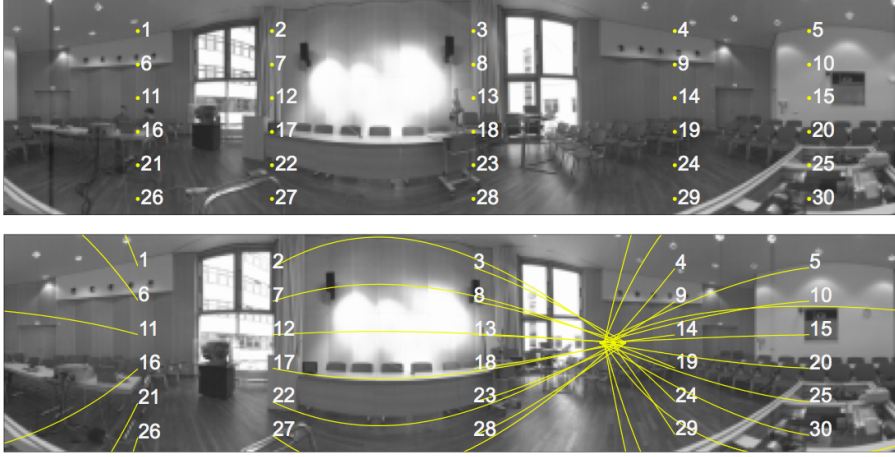
Figure 2.4. A pair of horizontally-aligned panoramas. Top: the source panorama with 30 test points labeled by '·' and indexed by numbers. Bottom: the destination panorama superimposed with the corresponding epipolar curves.

which is as stated in the corollary.   □

If panoramic images are taken at identical elevation then they are *horizontally-aligned panoramas*, and the epipolar curve equation for such a pair (which is also leveled) can be further simplified into

$$y_2 = y_1 \left(\frac{f_2}{f_1} \right) \left(\frac{R_2 \sin \omega_2 - R_1 \sin(\sigma_2 - \alpha_1) - t_x \cos \sigma_2 + t_z \sin \sigma_2}{-R_1 \sin \omega_1 + R_2 \sin(\sigma_1 - \alpha_2 - \phi) - t_x \cos \sigma_1 + t_z \sin \sigma_1} \right)$$

where $\sigma_1 = (\alpha_1 + \omega_1)$ and $\sigma_2 = (\alpha_2 + \omega_2 + \phi)$. This equation can be derived from Corollary 2.1 by setting $t_y = 0$.

An example of a pair of panoramic images, being 'almost'[4] horizontally-aligned, is shown in Figure 2.4. These panoramas were captured at DLR by the high-resolution, three-line line camera WAAC (Sandau and Eckardt, 1996; Reulke and Scheele, 1998) in a complete $360°$ progressive scan. Each sensor line has 5,184 elements. The associated principal angles for both images are equal to $25°$. The effective focal length of the line-camera is $21.7mm$ for the center sensor line, and $23.94mm$ for its two symmetric sensor lines. Both the effective focal length and the principal angle had been exactly calibrated using on-site DLR facilities.

The off-axis distances for the panoramic pair are both equal to $100mm$, and the associated rotation axes of this panoramic pair are $1m$ apart;

---

[4] With a possible error in elevations due to a manual movement of the image acquisition system.
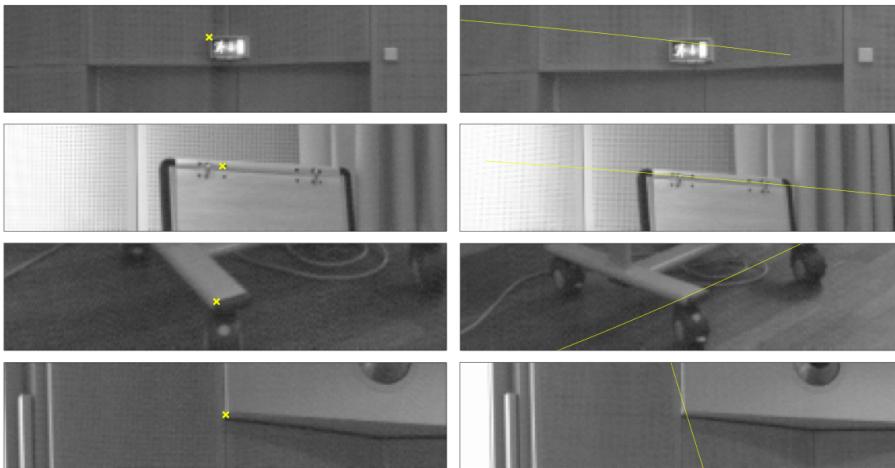
Figure 2.5.   Close-ups of image points in the destination panorama, and corresponding epipolar curves as calculated by the provided equation.

besides careful measurement there might be some error involved. The line-camera took 22,000 line images each for two complete 360° scans at both positions. Most of the calculated epipolar curves pass through expected (corresponding) image points in the destination panorama. Close-up views of selected points (at "corners") and their corresponding epipolar curves are shown in Figure 2.5. This is an experimental illustration of the correctness of the provided epipolar curve equation for horizontally-aligned leveled panoramas.

2.2.2. CO-AXIS PANORAMIC PAIR

Two panoramas whose axes coincide form a *co-axis panoramic pair*. (The implementation of such a camera configuration is reasonably straightforward by using a tripod.) The co-axis constraint eliminates two rotational and two translational parameters. [The co-axis constraint is also applied for catadioptric cameras, see (Southwell et al., 1996; Gluckman et al., 1998; Nene and Nayar, 1998; Petty et al., 1998).] The epipolar geometry of a co-axis panoramic pair is characterized by the following:

COROLLARY 2.2.   *Let (x_1, y_1) and (x_2, y_2) be a pair of corresponding image points in a co-axis pair of panoramas. Given x_1 and y_1, we have*

$$y_2 = \frac{y_1 \left(\frac{f_2}{f_1} \right)(R_2 \sin \omega_2 - R_1 \sin(\sigma_2 - \alpha_1)) - t_y f_2 \sin(\sigma_2 - \sigma_1)}{R_2 \sin(\sigma_1 - \alpha_2 - \phi) - R_1 \sin \omega_1}$$

where $\alpha_1 = \frac{2\pi x_1}{\mu W_1}$, $\alpha_2 = \frac{2\pi x_2}{\mu W_2}$, $\sigma_1 = (\alpha_1 + \omega_1)$ and $\sigma_2 = (\alpha_2 + \omega_2 + \phi)$, and the angle ϕ determines the rotation with respect to the y-axis.

Proof The equation can be derived from Corollary 2.1 by setting $t_x = 0$ and $t_z = 0$.   □

From this example we can conclude that epipolar curves of a co-axis pair can coincide with image columns for specific camera settings.

Now consider a pair of co-axis panoramas where associated centers coincide; this is a *concentric panoramic pair*. The epipolar curve equation of a concentric panoramic pair further simplifies to the following:

$$y_2 = \frac{y_1 \left(\frac{f_2}{f_1} \right) (R_2 \sin \omega_2 - R_1 \sin(\sigma_2 - \alpha_1))}{R_2 \sin(\sigma_1 - \alpha_2 - \phi) - R_1 \sin \omega_1} \tag{10}$$

This is obtained when using $t_y = 0$ in the equation given in Corollary 2.2.

Practically, concentric panoramic pairs can be produced in a very simple way; for example by rotating a matrix camera; see (Ishiguro et al., 1992; Shum and He, 1999). In this case a set of panoramic images may be generated from different columns of the matrix images, where every fixed column generates exactly one of these panoramic images.

An example of a concentric panoramic pair taken by the line camera WAAC is shown in Figure 2.6. The technical data are the same as for the leveled case, besides the following modifications: the off-axis distance for
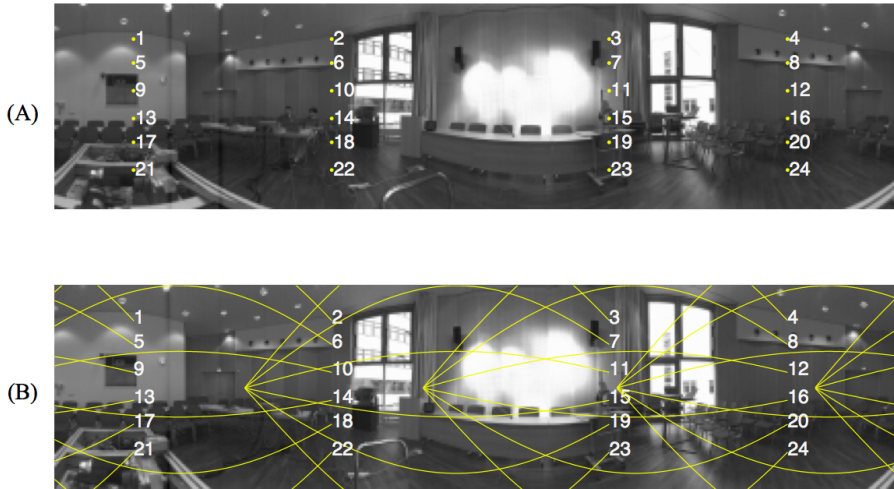

Figure 2.6. A pair of concentric panoramas. Top: the source panorama with 24 test points labeled by '·' and indexed by numbers. Bottom: the destination panorama superimposed with corresponding epipolar curves.

the source panorama of the pair is equal to $100mm$, and $0mm$ for the destination panorama of the pair. The calculated epipolar curves, superimposed on the destination image, show again incidence with corresponding points.

2.2.3. SYMMETRIC PANORAMIC PAIR

Two concentric panoramas whose associated off-axis distances, effective focal lengths, and angular units are pairwise identical, and whose principal angles sum up to $360°$ (i.e., both angles can be denoted as ω and $-\omega$) are called a *symmetric panoramic pair.*

These panoramic pairs have applications in stereo panoramic imaging (computational stereo and stereo viewing); they possess a simple epipolar geometry as characterized by the following:

COROLLARY 2.3. *Epipolar curves are straight lines and coincide with image rows, for any symmetric pair of panoramic images.*

Proof This fact follows from the epipolar curve equation in Corollary 2.2 by setting $t_y = 0$, $\phi = 0$, $f_1 = f_2$, $R_1 = R_2$, $W_1 = W_2$, and $\omega_2 = (2\pi - \omega_1)$. In this case, we have

$$
\begin{aligned}
y_2 &= y_1 \left(\frac{R_1 \sin(2\pi - \omega_1) - R_1 \sin(\alpha_2 - \alpha_1 + 2\pi - \omega_1)}{-R_1 \sin \omega_1 - R_1 \sin(\alpha_2 - \alpha_1 - \omega_1)} \right) \\
&= y_1 \left(\frac{-\sin \omega_1 - \sin(\alpha_2 - \alpha_1 - \omega_1)}{-\sin \omega_1 - \sin(\alpha_2 - \alpha_1 - \omega_1)} \right) \\
&= y_1
\end{aligned}
$$

The value of y_2 is identical to y_1, regardless of the values of all other (not yet specified) parameters. This implies that the epipolar curve, corresponding to image point (x_1, y_1), coincides with the image row y_2 on the destination image with $y_1 = y_2$. Thus, the epipolar curve is a straight line. $\square$
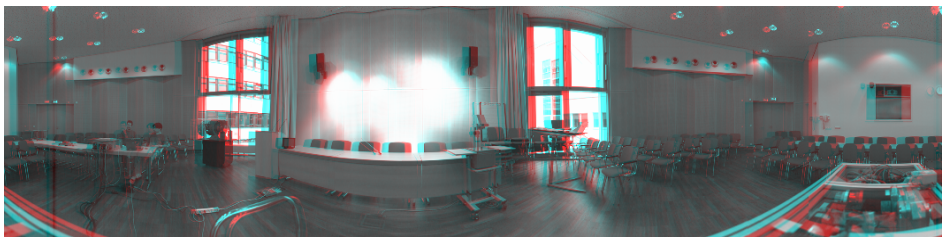

Figure 2.7.   Anaglyph of a symmetric panoramic pair. It requires a presentation in color and anaglyphic eyeglasses for 3D viewing.

In consequence of Corollary 2.3 it follows that stereo-matching algo-
rithms previously developed for pinhole binocular stereo, such as (Marr and
Poggio, 1979; Barnard and Fischler, 1982; Ohta and Kanade, 1985; Cox,
1994; Šára, 1999; Gimelfarb, 2002), are reusable. The corollary also charac-
terizes symmetric pairs as being stereoscopic-viewable without further pro-
cessing (e.g., using anaglyphic techniques or polarized light). An anaglyphic
example of a symmetric pair is shown in Figure 2.7.

SPATIAL SAMPLING

Spatial sampling describes how a 3D space is sampled by stereo pairs of images, without considering geometric or photometric complexities of 3D scenes. This chapter presents studies on spatial sampling for *stereo panoramas* which are a pair of panoramic images which only differ in the chosen value of the principal angle ω. Symmetric panoramas are a special case of stereo panoramas. Stereo panoramas received attentions in the context of various applications; see, for example, (Ishiguro et al., 1992; Murray, 1995; Huang and Hung, 1998; Wei et al., 1998a; Peleg and Ben-Ezra, 1999; Shum et al., 1999; Huang et al., 2001a; Huang et al., 2001c; Wei et al., 2002; Wei et al., 2002a).

Consider a stereo panorama $E_{\mathcal{P}_R}(R, f, \omega_L, \gamma)$ and $E_{\mathcal{P}_L}(R, f, \omega_R, \gamma)$, with $0 \leq \omega_R < \omega_L < 2\pi$. Without loss of generality, we call the panorama that is associated to the smaller (larger) value of the principal angle the right (left) image. When it is necessary to refer to values of the parameters, we only refer to the right image's parameters for reducing repetitions. In the symmetric case (i.e., $\omega_L = 2\pi - \omega$, and $\omega_R = \omega$), we only consider ω between 0 and π. This chapter will mostly consider stereo panoramas which are symmetric; non-symmetric cases are explicitly identified as such.

The first section of this chapter is about sampling structures of stereo panoramic cameras. The second section discusses sample resolution. The final section computes different sample distances and discusses spatial dependencies of sample density.

3.1. Sampling Structure

A *spatial sample* is defined by an intersection of two projection rays, one normally defined by the right and the other by the left camera. However, exceptions may occur: two projection rays forming a spatial sample may also be defined by the same panorama, see Subsection 3.1.2. The *structure of spatial samples* describes their distribution in 3D space.

Unlike in the approach by (Shum et al., 1999), where only the sampling

structure of the tangential projection direction (i.e., $\omega = \pi/2$) is discussed, we investigate panoramic sampling structures for the omnidirectional [i.e., $\omega \in [0, 2\pi)$] case.

Due to basic differences in sampling structure characteristics, this section is divided into two subsections, addressing the *outward case* defined by $0 \leq \omega \leq \pi/2$, and the *inward case* defined by $\pi/2 < \omega \leq \pi$.

3.1.1. OUTWARD CASE

In the outward case, no projection ray passes through the interior of the base cylinder, see Figure 3.1. This Figure illustrates top views of spatial sample formations of symmetric panoramas: (A) is the camera model, (B) and (C) show projection rays emitting from projection centers on the base circles, where (B) is the case of the right and (C) of the left stereo panorama, (D) is just the superimposition of (B) and (C), and (D) sketches the basic structure of stereo samples [i.e., of all intersection points in (D)], which form *supporting concentric circles* (actually: *supporting concentric cylinders* in
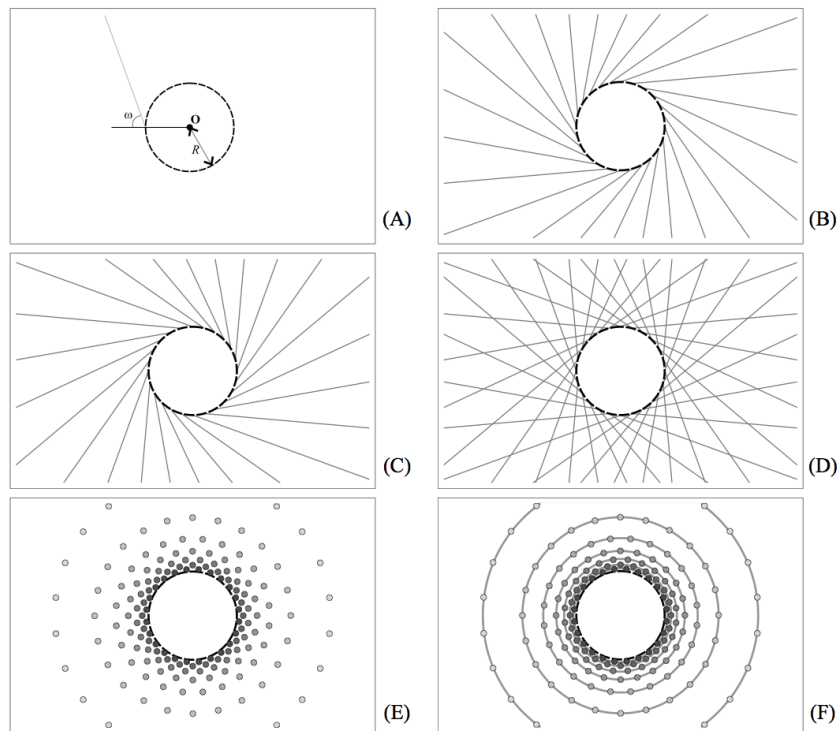

Figure 3.1.   Sampling structure in a symmetric outward case.

3D). The innermost (black) circle in (D) is the base circle; one should not confuse it with a supporting concentric circle. The radiuses of concentric circles increase non-linearly.

Motivated by the fact that samples are layered in depth (= distance from **O**), we refer to these supporting concentric circles (cylinders, in 3D) also as *depth layers*.

Figure 3.2 is a 3D visualization of the sampling structure already illustrated by Figure 3.1 (F), but now also indicating the 3D distribution of samples.

Samples are drawn at different sizes (larger as they are further away from **O**), and in different gray levels for different depth layers. The structure of all depth layers can be described as a set of straight concentric cylinders whose top and bottom frontiers are incident with a pair of co-axis hyperboloids which are symmetric to the base plane. This observation can also be confirmed by the fact that the epipolar surface for stereo panoramas is a half-hyperboloid (Seitz, 2001).

The density of depth layers increases inversely with the distance to the base cylinder. (This will be different for the inward case.) A change of the off-axis distance R has the effect of increasing (reducing) density of depth layers towards (away from) **O**. For example, a large value of R allows more depth samples for a distant object in a scene, compared to a small value of
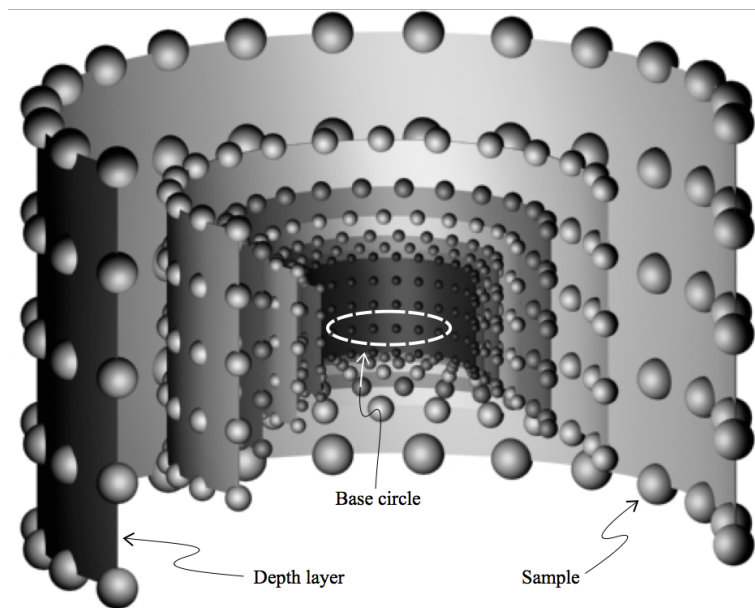

Figure 3.2.   3D view of sampling structure for a symmetric outward case.
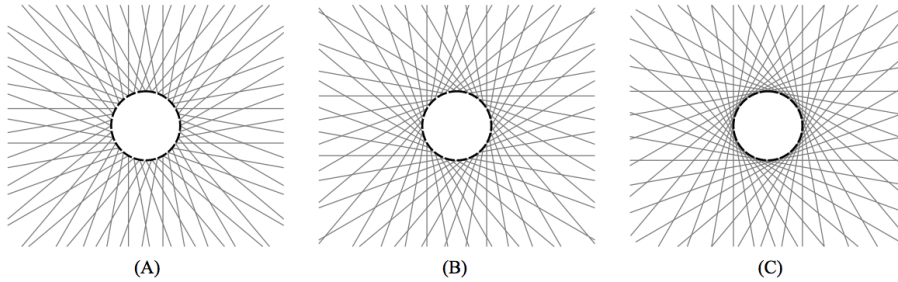
Figure 3.3. Sampling patterns of three symmetric outward panoramas. (A) $\omega = 30°$, (B) $\omega = 60°$, and (C) $\omega = 90°$.

R. This effect is analogous to changes in the base distance between both cameras in pinhole binocular stereo. Note: a change in R— does not alter the number of depth layers, just their spatial distribution.

A change of the principal angle ω alters the total number of depth layers in 3D space (an exact analysis will be provided later). Figure 3.3 shows three examples of sampling structures for different angles ω (for 30°, 60°, and 90°), where R is assumed to remain constant.

The number of depth layers increases as ω increases in the interval which defined the outward case. A similar effect is known for pinhole vergenced stereo pairs, where an increase in vergence angle increases the number of (potential) depth levels in 3D space, and thus also the (potential) accuracy in stereo reconstruction. However, pinhole vergenced stereo pairs suffer from the change in epipolar geometry compared to *standard stereo geometry* (i.e., parallel optical axes, and image row y in left image colinear to image row y in right image, for all image rows). Stereo panoramas still have all epipolar lines on their image rows, for any angle ω. This is a remarkable advantage of stereo panoramas compared to pinhole stereo pairs.

We conclude that cardinality and density distribution of spatial samples are influenced by the chosen values of ω and R, without leaving (for any chosen pair of values!) the space of stereo-viewable panoramas, which also allow the use of computational stereo as designed for standard (pinhole) stereo geometry. (This advantage also allows control of spatial sampling in dependence of the spatial complexity of the scene; see Chapter 7.)

3.1.2. INWARD CASE

Now we assume a principal angle ω greater than 90° and less than or equal to 180°. All projection rays intersect the interior of the base cylinder.

The inward case has a sampling structure which is more complex than the one for the outward case. It also has various geometric features which
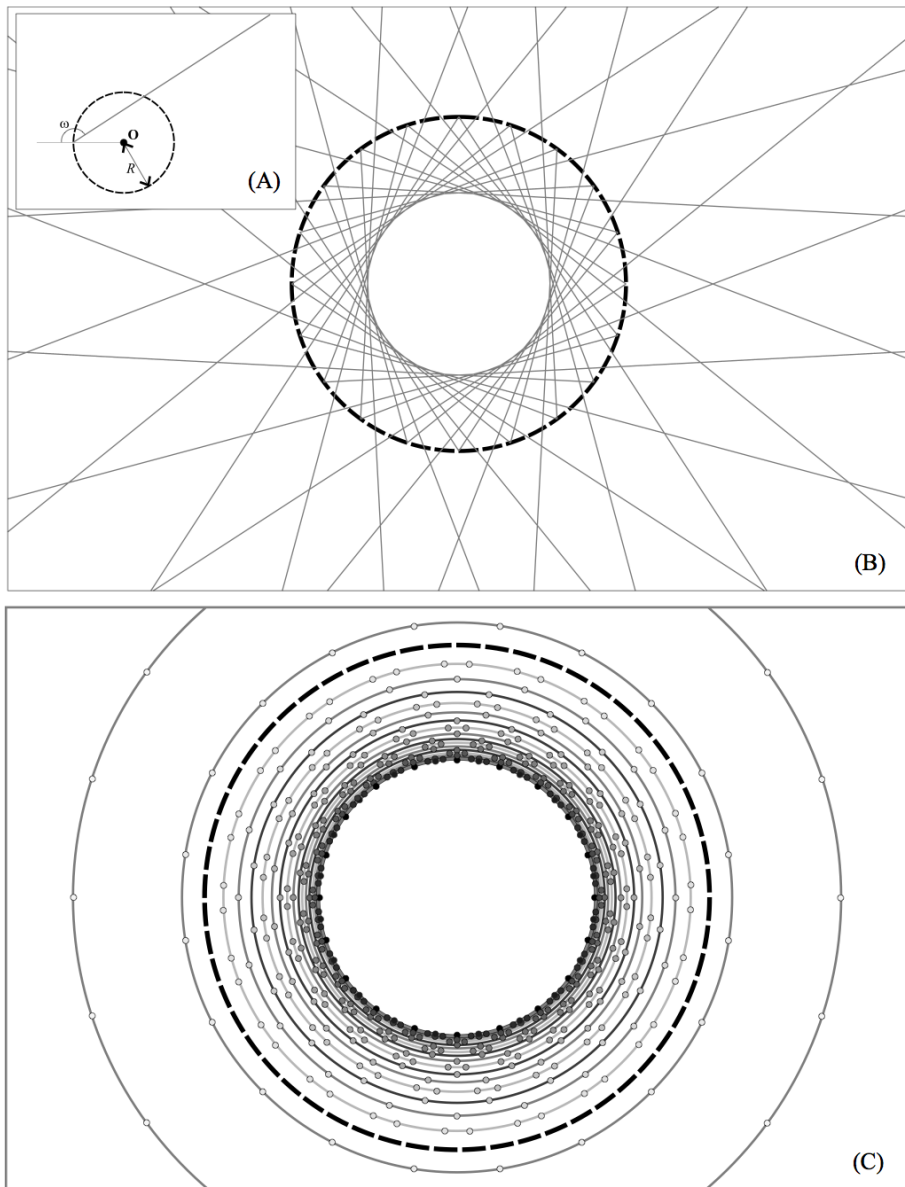
Figure 3.4. Sampling structure of a panoramic camera in symmetric inward case.

characterize it as being of potential value for applications including scene reconstruction for close-range (indoor) scenes, design of calibration objects, or shape reconstruction of 3D objects.

Figure 3.4 illustrates the inward case of a panoramic camera. The small

insert (A) shows a single projection ray in a top view of the base cylinder, (B) shows the geometry of multiple projection rays (which all first intersect the interior of the base cylinder shown as bold dashed circle, and then continue into its exterior towards infinity), and (C) illustrates the supporting concentric circles (i.e., cylinders in 3D) for this case.

There are three zones of sampling structures (listed outwards, starting at the center): (1) a *sample-free zone* enclosed by the *inner surface* tangential to all projection rays, followed by (2) an *in-between zone* enclosed by the base cylinder, and then (3) the zone outside of the base cylinder.

In this subsection we discuss first the sampling structure of the in-between zone, then that of the sample-free zone, but not that of the zone outside of the base cylinder because it allows similar (general) observations as discussed for the outward case. (A formal analysis follows in the next section.)

Figure 3.4 (C) is an enlarged representation of Figure 3.4(B). The dashed circle is the base circle; one should not confuse it with a depth layer (i.e., a supporting concentric circle). There are three kinds of depth layers in the in-between zone. One is formed by intersections of projection rays before the rays intersect the tangential inner surface, and those layers are shown in gray. Another kind is formed by intersections of projection rays after the rays intersected the tangential inner surface, shown in dark gray. Finally there are depth layers shown in light gray; these are created by two rays where one was not yet incident with the inner surface, but the other ray was. The first two kinds are *identical-type depth layers*.

Potential depth samples are evenly distributed on identical-type depth layers. The third kind (of opposite-type depth layers) is characterized by uneven distributions except under a special condition (to be discussed later).

More importantly, only identical-type depth layers of inward stereo panoramas follow the symmetric principle of epipolar geometry which ensures that epipolar lines coincide with image rows. Opposite-type depth layers contain potential samples which are defined by only one image of the stereo pair. In these cases an image point has a corresponding point in the same image, that means, the epipolar curve is also defined in the same image, and not a line anymore which coincides with an image row.

In general we would assume that a sample in the in-between zone is uniquely defined by two rays which intersect at this point. However, when the angular unit γ is, for example, a factor of $2\omega - 180°$, then a *multiple sample* is defined by at least two intersection points; it can be defined by four at most where two are identical-type and two are opposite-type. Figure 3.5 shows an example of this special case, where $\omega = 160°$ and $\gamma = 10°$. Note that under this special condition, *all* samples are uniformly distributed
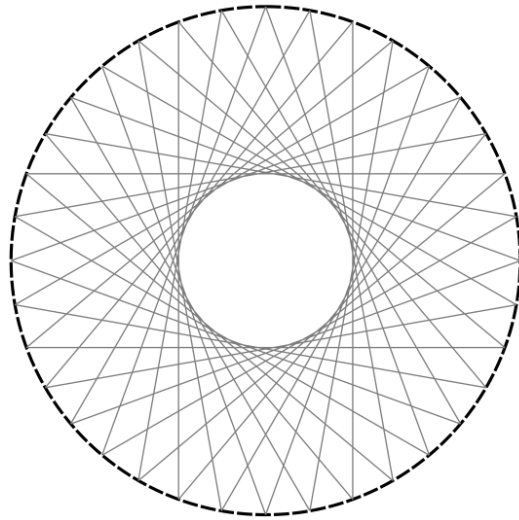
Figure 3.5.   Special case of an inward sampling structure where samples can be defined by multiple intersection points of rays..

on their depth layers, including opposite-type depth layers. A point in 3D can thus be stereo-sampled up to four times. The occurrence of this ideal case is constrained by occlusions in captured scenes.

Whether opposite-type samples just define a problem for stereo applications of inward stereo panoramas, or also allow a particular utilization, has not yet been studied. A possible application is the design of calibration objects for panoramic camera calibration. A special calibration object can be designed such that calibration marks on the calibration object are at
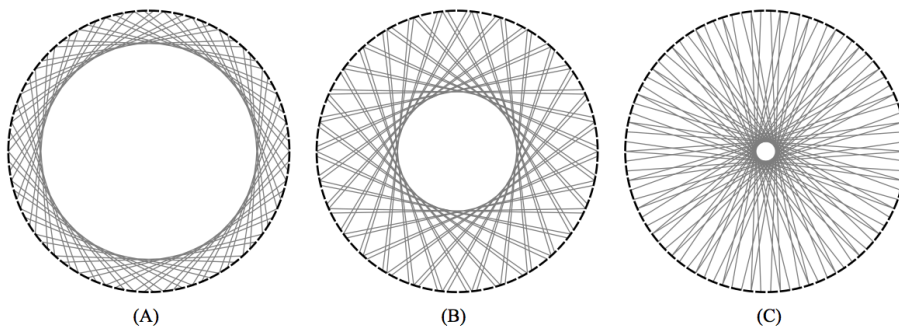

(A)   (B)   (C)

Figure 3.6.   Inward sampling patterns for stereo panoramic pairs with (A) $\omega = 130°$, (B) $\omega = 155°$, and (C) $\omega = 175°$.

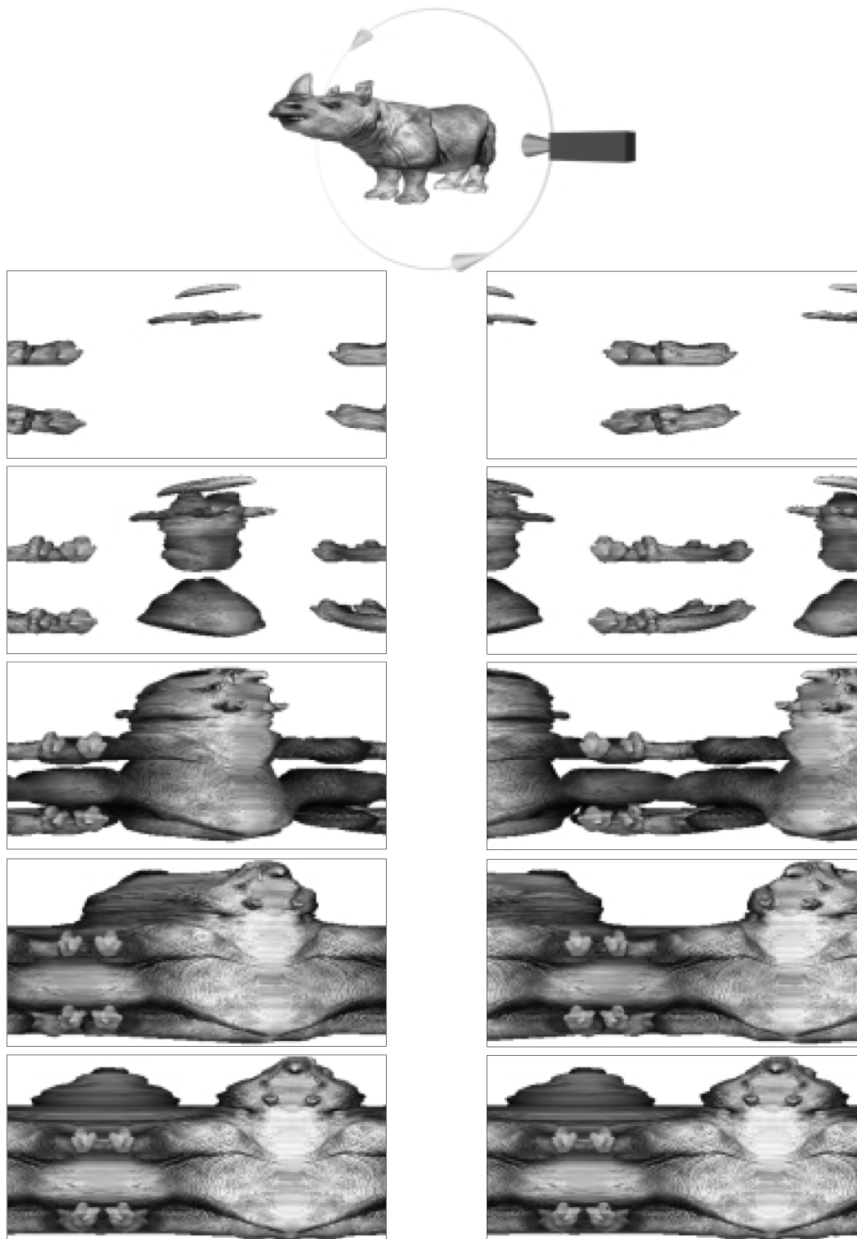*Figure 3.7.* Top: a synthetic rhino. Row by row: five stereo panoramic pairs, with (top to bottom) (ω_L, ω_R) equals to $(155°, 205°)$, $(160°, 200°)$, $(165°, 195°)$, $(172°, 188°)$, or $(179°, 181°)$.

positions sampled twice in a single (!) panorama. This may contribute to calibration accuracy. Moreover, accurate camera calibration requires the projection of a calibration object that covers most of the area of the captured image. Obviously, compared to the outward case, the inward case allows much smaller calibration objects (with a diameter less than R).

The density of depth layers increases towards the inner surface of the sample-free zone (rather than towards the base cylinder as in the outward case). A change of the off-axis distance R has a similar effect as in the outward case (i.e., no alteration of numbers of samples, but a dynamic change of the density pattern). A change of the principal angle ω, however, allows different observations compared to the outward case.

Figure 3.6 illustrates three sampling structures for ω equal to $130°$, $155°$, or $175°$; R remains constant for all three angles. A larger value of ω increases the number of samples. But note that a less vergenced angle reduces accuracy in stereo reconstruction. The value of ω has effect on the size of the sample-free zone; see Figure 3.6. This can be formally expressed.

The sample-free zone is enclosed by the inner surface (a cylinder) which is tangential to all projection rays. Let r be the radius of this cylinder. It satisfies the following relation:

$$r = R \cdot \sin(|180° - \omega|)$$

The off-axis distance R is (just) a scaling factor for r. The principal angle ω however, offers more flexibility.

This is illustrated by Figure 3.7 by (symmetric) stereo panoramas. A synthetic rhino is placed into the base circle of the panoramic camera, and a sequence of stereo panoramas is acquired using different values of ω. The figure shows stereo pairs where (ω_R, ω_L) is equal to $(155°, 205°)$, $(160°, 200°)$, $(165°, 195°)$, $(172°, 188°)$, or $(179°, 181°)$.

A stereo reconstruction (e.g., of surface "slices" of the rhino) may be based on individual stereo panoramas, and reconstruction accuracy may be enhanced by utilizing interrelations among reconstructions obtained from individual pairs. This finally supports accumulated stereo reconstruction of the whole (visible) surface.

3.2. Spatial Resolution

The previous section discussed the general geometric structure of potential samples in stereo panoramas. This section focuses on a more specific issue, namely the *spatial resolution* which is defined by the number of samples per volume element.

Since sampling density is not uniform in 3D space, spatial resolution depends upon position. This section provides a first answer, and a more

detailed analysis (characterizing distances between samples) follows in the next section.

3.2.1. INDEXING SYSTEM

The following (unified) indexing system for outward and inward case is such that calculations of sampling resolution or sample distance will not depend anymore on 'outward' or 'inward', instead just on discrete indices (i, j, k) of samples.

Every sample in 3D space is indexed as (i, j, k), where index i identifies uniquely the direction (i.e., one of finitely many intervals of directions of rays emerging at $\mathbf{O}$) to the sample, j represents uniquely the elevation of the sample (in its depth layer) with respect to the base plane, and k specifies the depth layer of the sample. Index i starts with value 0 at a predefined direction and increases clockwise. Index j is not equal to the elevation; it just numbers samples starting with value 0 at the base plane, and decreasing upward or increasing downward. Index k starts with value 0 at the base cylinder and increases for samples with their distance to the projection center (note: this distance increase is also uniquely specified for the inward case). The indexing system is illustrated in Figure 3.8 for the outward case.
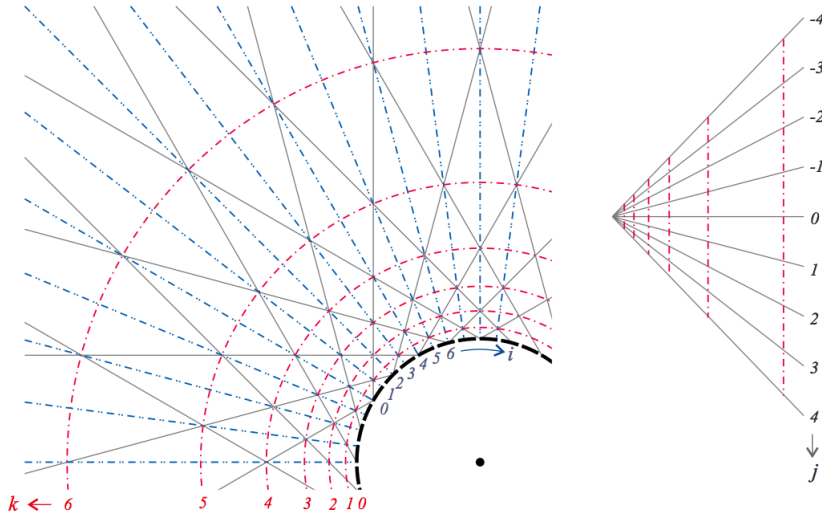

Figure 3.8.   Indexing system of sampling structures. Left: a partial top view shows indices i (indices of sectors, each between two dashed gray lines) and k (index of depth layer). Right: index j is illustrated for one depth layer of a side view of a single (perspective) projection.

The dashed black bold arc on the left of this figure is part of the base circle. Gray solid lines represent projection rays into the 3D space. Gray dashed straight lines represent sectors of directions indexed by i. Gray concentric dashed arcs indicate different indices of k (i.e., of depth layers).

The right of Figure 3.8 illustrates index j. Vertical gray dashed lines show different depth layers. The value of j is zero at the base plane; positive values are downwards.

An integer triple (i, j, k) is indexing an existing sample iff the values of i and k are either both odd or both even (with an exception for $k = 0$; in this case we also assume $j = 0$). Index $(i, 0, 0)$, with i even, refers to a projection center on the base circle.

3.2.2. COMPUTATION OF RESOLUTION

Recall that W is the number of image columns of a panorama, and H the number of image rows.

Following above definitions, index i starts at zero and goes to $2W - 1$. If i exceeds $2W - 1$ then we consider it modulo $2W$.

Index j goes from $\frac{-(H-1)}{2}$ to $\frac{(H-1)}{2}$ if H is odd, or from $\frac{-(H-2)}{2}$ to $\frac{H}{2}$ if H is even.

The interval of possible k values is more difficult to be specified. Obviously, index k goes from zero to a value k_{max} which specifies the maximum number of depth layers. This number can be calculated from principle angle ω and unit angle γ as follows:

$$k_{max} = \left\lfloor \frac{2\omega}{\gamma} \right\rfloor$$

Note that 2ω is the angular (i.e., angle with center point at $\mathbf{O}$) distance between two projection centers whose associated projection rays are parallel. For a symmetric panorama we have to consider ω between 0 and π only. (If $\omega = \pi$, then $2\omega = 2\pi \equiv 0$ and $k_{max} = 0$.) Thus we can rewrite above equation for k_{max} as follows:

$$k_{max} = \left\lfloor \frac{2(\omega \bmod \pi)}{\gamma} \right\rfloor$$

Alternatively, k_{max} can also be determined by ω and W as follows:

$$k_{max} = \left\lfloor \frac{(\omega \bmod \pi)W}{180°} \right\rfloor \tag{1}$$

The discussion above has identified the following extreme cases:

PROPOSITION 3.1. *A symmetric panorama with ω equals to 0 or π does not allow any spatial sample.*

The combination of both representations of k_{max} leads to the following theorem for symmetric panoramas. The total number of spatial samples of a stereo panorama is also called its *spatial sampling resolution.*

THEOREM 3.1. *Given a symmetric panorama of image resolution $W \times H$ where the principal angle ω (of the right camera) is in the interval $(0, \pi)$. The spatial sampling resolution of such a panorama is equal to*

$$W \times H \times \left\lfloor \frac{\omega W}{\pi} \right\rfloor \qquad\qquad (2)$$

Proof There are $2W$ different values of i (from zero to $2W - 1$). There are H different values of j according to the definition of this index. The value of index k goes from zero to $\lfloor \frac{\omega W}{\pi} \rfloor$, thus there are $\lfloor \frac{\omega W}{\pi} \rfloor + 1$ different values of k.

The total number of spatial samples is thus upper bounded by the product of these three values $2W$, H, and $\lfloor \frac{\omega W}{\pi} \rfloor + 1$. However, there are only W spatial samples for each pair of values of j and k (see Figure 3.8), and there are no samples for $k = 0$. Therefore, the total number of spatial samples is equal to $W \times H \times \lfloor \frac{\omega W}{\pi} \rfloor$. $\qquad\qquad \square$

COROLLARY 3.1. *The off-axis distance R of a symmetric panorama has no impact on the spatial sampling resolution.*

COROLLARY 3.2. *The spatial sampling resolution of a symmetric panorama increases as ω increases towards π.*

In the inward case, the spatial sampling resolution increases with ω following the last corollary, but the samples are clustered more and more towards the center of the base circle; see Figure 3.6; the number of samples outside of the base cylinder is decreasing with increasing ω.

COROLLARY 3.3. *In the outward case, the spatial sampling resolution of a symmetric panorama reaches a maximum at $\omega = 90°$.*

Proof By definition of the outward case (i.e., $\omega \in [0°, 90°]$). $\qquad\qquad \square$

The last corollary coincides with results in (Shum et al., 1999).

3.3. Distances Between Spatial Samples

Samples are non-uniformly distributed in 3D space. Figure 3.9 illustrates a local neighborhood of samples (shown as differently shaded shapes) around
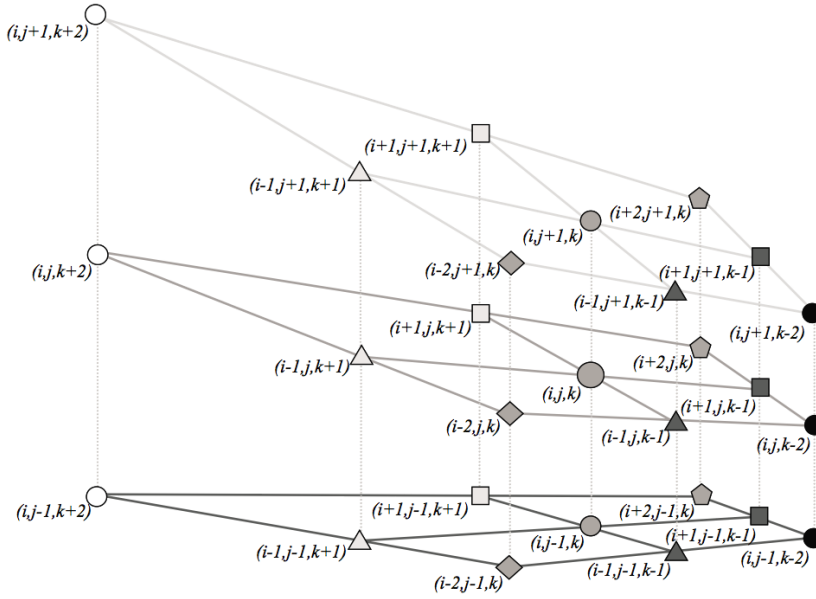
Figure 3.9. Indexed samples in the neighborhood of sample (i, j, k).

a sample (i, j, k). As stated above, not every triple (i, j, k) has a corresponding sample. Positions of samples can be identified with a regular grid where each grid point (i.e., sample) has exactly six adjacent samples. The definition of adjacency follows below (which does not correspond to edges shown in Figure 3.9).

When adjusting an image acquisition system to a particular scene it might be of value to know the exact distance between adjacent samples at a specified *depth* (i.e., distance from the camera).

Sample distance denotes the distance between two adjacent samples; it is undefined for pairs of non-adjacent samples. This section defines sample distances for stereo panoramas, derives related formulas, discusses changes in sample distances depending on depth or depth layer.

3.3.1. BASIC DEFINITIONS

Figure 3.9 shows projection rays as solid gray lines. As always, samples are at intersections of those rays. We use five different shapes to indicate different i values, five different levels of shadings to indicate different depth layers (i.e., different k values), and three 3×3 grids (i.e., top, middle, and bottom) with lines of different gray levels to indicate the three height values of all shown samples (i.e., different j values).
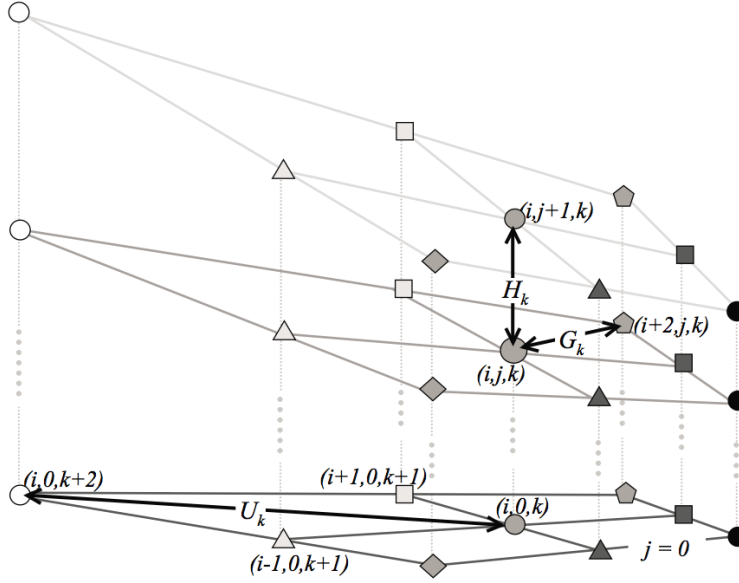
Figure 3.10.   Illustration of horizontal, vertical, and depth sample distances.

DEFINITION 3.1.   *Sample (i, j, k) is horizontally adjacent to sample $(i + 2, j, k)$, vertically adjacent to sample $(i, j+1, k)$, and depth-adjacent to sample $(i, j, k+2)$. Two samples are adjacent if one of both is either horizontally, vertically, or depth-adjacent to the other.*

Adjacency is thus an irreflexive and symmetric relation. Each sample is adjacent to six other samples. Horizontal, vertical, or depth-adjacency is asymmetric and irreflexive, and these three relations define

 — *horizontal sample distance G_k* between sample (i, j, k) and its horizontally adjacent sample,
 — *vertical sample distance H_k* between sample (i, j, k) and its vertically adjacent sample,
 — *depth sample distance U_k* between sample (i, j, k) and its depth-adjacent sample after projecting both into the base plane (i.e., distance between $(i, 0, k)$ and $(i, 0, k + 2)$).

The distances G_k, H_k and U_k are constant for all samples in the same depth layer; thus we do not have to add variables i or j. For an illustration of sample distances, see Figure 3.10 (which follows the graphical conventions of Figure 3.9).

In order to find sample distances to a reference sample at a particular distance, we need one more definition:
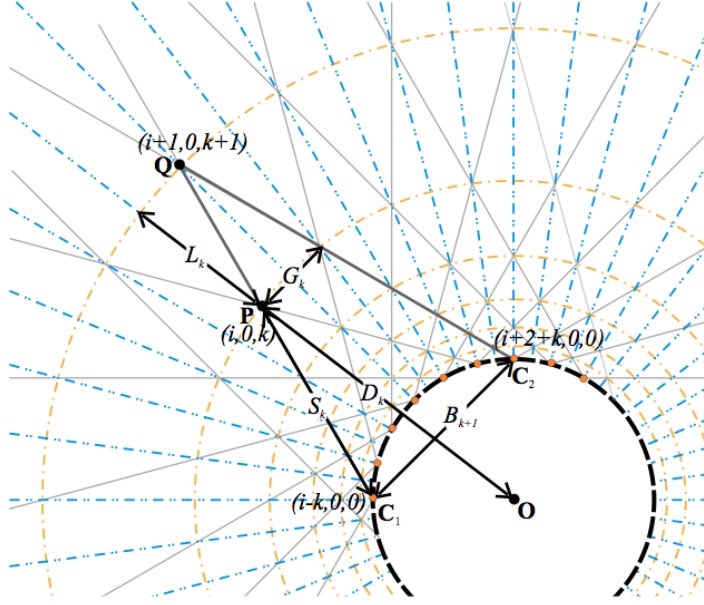
Figure 3.11. Auxiliary distances B_k and S_k, used for calculating sample distances G_k, H_k, and U_k of a reference sample (i, j, k) at distance D_k.

DEFINITION 3.2. *The depth D_k of a sample (i, j, k) is the distance between sample $(i, 0, k)$ and the center $\boldsymbol{O}$ of the base circle.*

Depth is defined on the base plane with $j = 0$. Index i is not needed for specifying D_k because all samples in one depth layer have a constant depth.

Figure 3.11 illustrates the depth of a sample (i, j, k), which is the distance between $\mathbf{P}$ and $\mathbf{O}$, where point $\mathbf{P}$ denotes sample $(i, 0, k)$. Consider the triangle $\triangle \mathbf{P C_1 O}$. We know that $\overline{\mathbf{C_1 O}} = R$. Furthermore, we have $\angle \mathbf{P C_1 O} = \pi - \omega$ and $\angle \mathbf{C_1 O P} = \frac{k\gamma}{2}$. Thus, by the sine theorem, the value D_k is calculated as follows:

$$D_k = \frac{R \sin \omega}{\sin \left(\omega - \frac{k\gamma}{2} \right)} \tag{3}$$

3.3.2. HORIZONTAL SAMPLE DISTANCE

In order to calculate a horizontal sample distance, we define two auxiliary distances B_k and S_k; see Figure 3.11. B_k is the distance between both projection centers in the directional segments indexed by $(i, 0, 0)$ and $((i + 2k), 0, 0)$. It is defined on the base plane, in the interior of the base circle.

Distances B_k are simply the lengths of chords of the base circle, defined by k, and by elementary geometry known to be as follows:

$$B_k = 2R \sin\left(\frac{k\gamma}{2}\right)$$

S_k is the distance between the projection center with index $(i, 0, 0)$ and sample $(i + k, 0, k)$, where $k \neq 0$. It is also defined on the base plane and independent of i.

Figure 3.11 shows the distance S_k between points $\mathbf{P}$ and $\mathbf{C}_1$. Similar to the calculation of the depth of a sample, we consider the triangle $\triangle \mathbf{PC}_1\mathbf{O}$. Applying the sine theorem, the value S_k is calculated as follows:

$$S_k = \frac{R \sin\left(\frac{k\gamma}{2}\right)}{\sin\left(\omega - \frac{k\gamma}{2}\right)}$$

For calculating the horizontal sample distance at sample (i, j, k), we consider the triangle $\triangle \mathbf{QC}_1\mathbf{C}_2$ with vertices $(i + 1, j, k + 1)$, $(i - k, 0, 0)$, and $(i + 2 + k, 0, 0)$; see Figure 3.11. We have the following:

$$\frac{G_k}{B_{k+1}} = \frac{S_{k+1} - S_k}{S_{k+1}}$$

Thus, the horizontal sample distance G_k can be calculated as follows:

$$
\begin{aligned}
G_k &= B_{k+1} - \frac{B_{k+1} S_k}{S_{k+1}} \\
&= 2R \sin\left(\frac{(k+1)\gamma}{2}\right) - \frac{2R \sin\left(\frac{k\gamma}{2}\right) \sin\left(\omega - \frac{(k+1)\gamma}{2}\right)}{\sin\left(\omega - \frac{k\gamma}{2}\right)} \\
&= \frac{2R}{\sin\left(\omega - \frac{k\gamma}{2}\right)} \left(\sin\left(\frac{(k+1)\gamma}{2}\right)\left(\sin\omega \cos\left(\frac{k\gamma}{2}\right) - \cos\omega \sin\left(\frac{k\gamma}{2}\right)\right) \right. \\
&\quad \left. - \sin\left(\frac{k\gamma}{2}\right)\left(\sin\omega \cos\left(\frac{(k+1)\gamma}{2}\right) - \cos\omega \sin\left(\frac{(k+1)\gamma}{2}\right)\right) \right) \\
&= \frac{2R \sin\omega}{\sin\left(\omega - \frac{k\gamma}{2}\right)} \sin\left(\frac{(k+1)\gamma}{2} - \frac{k\gamma}{2}\right) \\
&= \frac{2R \sin\omega \sin\left(\frac{\gamma}{2}\right)}{\sin\left(\omega - \frac{k\gamma}{2}\right)}
\end{aligned}
$$

The first two diagrams in Figure 3.12 illustrate general relations between horizontal sample distances and depth layers. We assume $W = 5{,}000$ pixels
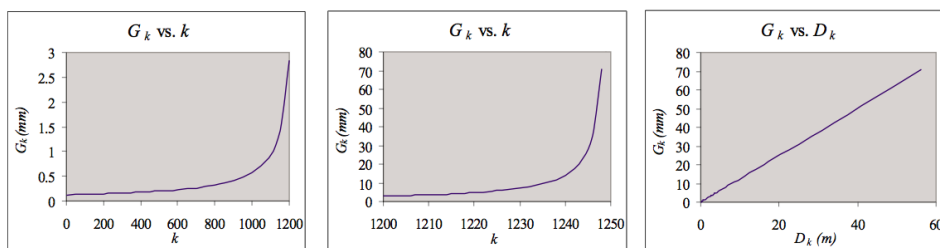
Figure 3.12. Diagrams for horizontal sample distances G_k versus depth layer index k (left and middle; note: two different scales) or D_k.

and let $R = 0.1m$ and $\omega = 45°$. Therefore, $\gamma = 360/5000 = 0.072°$. The number of depth layers is equal to 1,250 in this case.

The values of G_k are very small for $k < 1200$, and much larger otherwise. Therefore we split the diagram of G_k versus k into two parts: the one on the left shows values of k from 0 to 1,200, and the one in the middle of the figure shows the values of k from 1,200 to 1,248. We do not include G_k for $k = 1249$ or 1250 because G_{1249} and G_{1250} are extremely large numbers (and this would distract from the basic pattern shown in those diagrams). Both diagrams show exponential increase for horizontal sample distances, for increasing depth layers.

The horizontal sample distance at a sample can also be expressed in terms of depth. Combining Equation (3) with the equation for G_k, we have the following:

$$G_k = 2D_k \sin\left(\frac{\gamma}{2}\right)$$

We conclude that the horizontal sample distance of a sample is linearly proportional to its depth.

A diagram of G_k versus D_k is shown on the right of Figure 3.12. The maximum value of G_k is less than $7cm$, and there is no sample anymore if the distance D_k is greater than $60m$ (approximately).

3.3.3. VERTICAL SAMPLE DISTANCE

We have $H_k : S_k = \mu : f$, where μ is the size of a pixel (i.e., length of edge in the cell model). Thus, the value of H_k can be calculated as follows:

$$H_k = \frac{\mu R \sin\left(\frac{k\gamma}{2}\right)}{f \sin\left(\omega - \frac{k\gamma}{2}\right)}$$

The vertical sample distance at a sample can also be represented in terms of its depth value. From Equation (3), we obtain the following:

$$\sin\left(\omega - \frac{k\gamma}{2}\right) = \frac{R\sin\omega}{D_k}$$

and

$$\sin\left(\frac{k\gamma}{2}\right) = sin\left(\omega - \arcsin\left(\frac{R\sin\omega}{D_k}\right)\right)$$

Substituting these two terms into the equation for H_k, we have the following:

$$
\begin{aligned}
H_k &= \frac{\mu D_k \sin\left(\omega - \arcsin\left(\frac{R\sin\omega}{D_k}\right)\right)}{f\sin\omega} \\
&= \frac{\mu D_k \left(\sin\omega\cos\arcsin\left(\frac{R\sin\omega}{D_k}\right) - \cos\omega\frac{R\sin\omega}{D_k}\right)}{f\sin\omega} \\
&= \frac{\mu D_k \left(\sin\omega\sqrt{\frac{D_k^2 - R^2\sin^2\omega}{D_k^2}} - \frac{R\cos\omega\sin\omega}{D_k}\right)}{f\sin\omega} \\
&= \frac{\mu}{f}\left(\sqrt{D_k^2 - R^2\sin^2\omega} - R\cos\omega\right)
\end{aligned}
$$

Figure 3.13 shows diagrams of vertical sample distances with respect to different layers k (again: two different diagrams due to large variation of values) and depth values D_k. The used values of R, ω, and γ are as in the example for the horizontal case. Let $f = 35mm$ and $\mu = 0.01mm$. For such a configuration we observe that vertical sample distances are always smaller than horizontal sample distances at the same depth. Although the relation between H_k and D_k is not linear (as we see from the equation above), the diagram of H_k versus D_k also indicates that this relation is "almost linear".
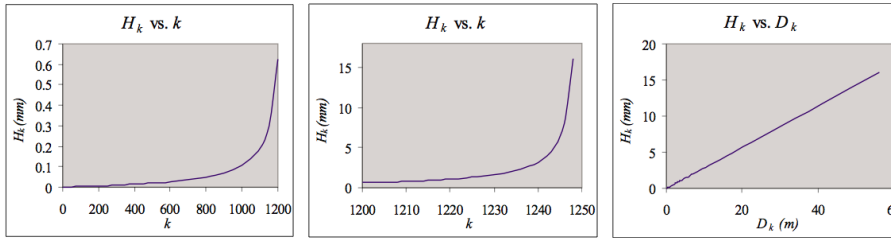

Figure 3.13. Diagrams for vertical sample distances H_k versus index k (left and middle; note: two different scales) or depth D_k.

3.3.4. DEPTH SAMPLE DISTANCE

DEFINITION 3.3. *The* depth layer distance L_k *at depth layer k is the distance $D_{k+1} - D_k$ between depth values of layers k and $k+1$.*

The value of L_k is as follows:

$$L_k = R \sin \omega \left(\frac{1}{\sin \left(\omega - \frac{(k+1)\gamma}{2} \right)} - \frac{1}{\sin \left(\omega - \frac{k\gamma}{2} \right)} \right)$$

It follows that the depth sample distance U_k at sample (i, j, k) is the sum of L_k and L_{k+1}. We have

$$U_k = R \sin \omega \left(\frac{1}{\sin \left(\omega - \frac{(k+2)\gamma}{2} \right)} - \frac{1}{\sin \left(\omega - \frac{k\gamma}{2} \right)} \right)$$

The depth sample distance at a sample can also be represented in terms of its depth value. Combining Equation (3) with the equation for U_k, we have the following:

$$
\begin{aligned}
U_k &= R \sin \omega \left(\frac{\sin \left(\omega - \frac{k\gamma}{2} \right) - \sin \left(\omega - \frac{(k+2)\gamma}{2} \right)}{\sin \left(\omega - \frac{k\gamma}{2} \right) \sin \left(\omega - \frac{(k+2)\gamma}{2} \right)} \right) \\
&= D_k \left(\frac{\sin \left(\omega - \frac{k\gamma}{2} \right) - \sin \left(\omega - \frac{(k+2)\gamma}{2} \right)}{\sin \left(\omega - \frac{(k+2)\gamma}{2} \right)} \right) \\
&= D_k \left(\frac{\sin \left(\omega - \frac{k\gamma}{2} \right)}{\sin \left(\omega - \frac{(k+2)\gamma}{2} \right)} - 1 \right) \\
&= D_k \left(\frac{R \sin \omega}{D_k \sin \left(\omega - \frac{k\gamma}{2} - \gamma \right)} - 1 \right) \\
&= \frac{R \sin \omega}{\sin(\omega - \frac{k\gamma}{2}) \cos \gamma - \cos(\omega - \frac{k\gamma}{2}) \sin \gamma} - D_k \\
&= \frac{R \sin \omega}{\frac{R \sin \omega \cos \gamma}{D_k} - \sin \gamma \sqrt{\frac{D_k^2 - R^2 \sin^2 \omega}{D_k^2}}} - D_k \\
&= \frac{D_k R \sin \omega}{R \sin \omega \cos \gamma - \sin \gamma \sqrt{D_k^2 - R^2 \sin^2 \omega}} - D_k
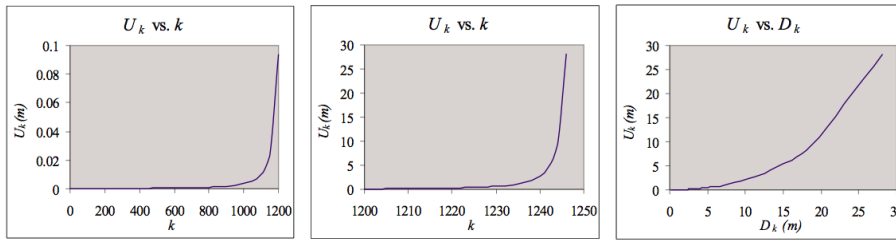\end{aligned}
$$

Figure 3.14.   Diagrams for depth sample distances U_k versus index k (left and middle; note: two different scales) or depth D_k.

Figure 3.14 shows diagrams of depth sample distances with respect to different layers k or depth values D_k. All parameter settings are as in the previous examples for horizontal or vertical sample distances. In difference to those cases, the value of U_k increases exponentially with increases in D_k.

References

Barnard, S. T., and M. A. Fischler: Computational stereo. *ACM Comput. Surv.*, **14**:553–572, 1982.

Chen, S. E.: QuickTimeVR - an image-based approach to virtual environment navigation. In Proc. *SIGGRAPH*, pages 29–38, 1995.

Cox, I. J.: A maximum likelihood n-camera stereo algorithm. In Proc. *Computer Vision Pattern Recognition*, pages 733–739, 1994.

Daniilides, K., and R. Klette (editors): *Computer Vision Beyond the Pinhole Camera.* Springer, Amsterdam, 2006.

Daniilides, K., and N. Papanikolopoulos (editors): *Panoramic Robots.* Special issue of *IEEE Robotics Automation Magazine*, Volume 11, December 2004.

Evers-Senne, J.-F., J. Woetzel, and R. Koch: Modelling and rendering of complex scenes with a multi-camera rig. In Proc. *European Conf. Visual Media Production*, pages 11–19, 2004.

Faugeras, O.: *Three-Dimensional Computer Vision: A Geometric Viewpoint.* The MIT Press, London, England, 1993.

Faugeras, O., and Q.-T. Luong. *The Geometry of Multiple Images.* The MIT Press, London, England, 2001.

Gimelfarb, G.: Probabilistic regularisation and symmetry in binocular dynamic programming stereo. *Pattern Recognition Letters*, **23**:431–442, 2002.

Gluckman, J., S. K. Nayar, and K. J. Thorek: Real-time panoramic stereo. In Proc. DARPA, pages 299–303, 1998.

Hartley, R. and A. Zisserman: *Multiple View Geometry in Computer Vision.* Cambridge Univ. Press, United Kingdom, 2000.

Hilbert, D., and S. Cohn-Vossen: *Anschauliche Geometrie.* Springer-Verlag, Berlin, 1932.

Huang, H.-C., and Y.-P. Hung: Panoramic stereo imaging system with automatic disparity warping and seaming. *Graph. Models Image Processing*, **60**:196–208, 1998.

Huang, F., S. K. Wei, and R. Klette: Geometric analysis of symmetric panorama imaging. In Proc. *Image Vision Comp. New Zealand*, pages 19–24, 2001a.

Huang, F., S. K. Wei, and R. Klette: Geometrical fundamentals of polycentric panoramas. In Proc. *Int. Conf. Computer Vision*, Volume I, pages 560–565, 2001b.

Huang, F., S. K. Wei, and R. Klette: Stereo reconstruction from polycentric panoramas. In Proc. *Robot Vision*, LNCS 1998, pages 209–218, 2001c.

Huang, F., S. K. Wei, and R. Klette: Rotating line cameras: model and calibration. Institute for Mathematics and its Applications, University of Minnesota, IMA Preprint Series, report 2104 (64 pages), March 2006.

Ishiguro, H., M. Yamamoto, and S. Tsuji: Omni-directional stereo. *IEEE Trans. Pattern Analysis Machine Intelligence*, **14**:257–262, 1992.

Kanatani, K.: *Geometric Computation for Machine Vision*. Oxford Univ. Press, New York, 1993.

Kang, S.-B., and R. Szeliski: 3-d scene data recovery using omnidirectional multibaseline stereo. *Int. J. Computer Vision*, **25**:167–183, 1997.

Klette, R., and R. Reulke: Modeling 3D scenes: paradigm shifts in photogrammetry, remote sensing and computer vision. Keynote, *IEEE Int. Conf. Systems and Signals*, 8 pages, conference CD, 2005

Klette, R., and K. Scheibe: Combinations of range data and panoramic images - new opportunities in 3D scene modeling. Keynote, in Proc. *IEEE Int. Conf. Computer Graphics Imaging Vision*, pages 3 - 10, 2005.

Klette, R., K. Schlüns, and A. Koschan. *Computer Vision: Three-Dimensional Data from Images*. Springer, Singapore, 1998.

Laveau, S., and O. Faugeras: 3-d scene representation as a collection of images. In Proc. *Int. Conf. Pattern Recognition*, pages 689–691, 1994.

Liu, G., R. Klette, and B. Rosenhahn: Structure from motion in the presence of noise. In Proc. *Image Vision Computing New Zealand* pages 138–143, 2005.

Mann, S., and R. W. Picard: Virtual bellows: Constructing high quality stills from video. In Proc. *IEEE Conf. Image Processing*, Volume I, pages 363–367, 1994.

Marr, D., and T. A. Poggio: A computational theory of human stereo vision. *Proc. R. Soc. Land. B.*, **204**:301–328, 1979.

McMillan, L., and G. Bishop: Plenoptic modeling: an image-based rendering system. In Proc. *SIGGRAPH*, pages 39–46, 1995a.

Murray, D.W.: Recovering range using virtual multicamera stereo. *Computer Vision Image Understanding*, **61**:285–291, 1995.

Nene, S. A., and S. K. Nayar: Stereo with mirrors. In Proc. *Int. Conf. Computer Vision*, pages 1087–1094, 1998.

Ohta, Y., and T. Kanade: Stereo by intra- and inter-scanline search using dynamic programming. *IEEE Trans. Pattern Analysis machine Intelligence*, **7**:139–154, 1985.

Peleg, S., and M. Ben-Ezra: Stereo panorama with a single camera. In Proc. *Computer Vision Pattern Recognition*, pages 395–401, 1999.

Peleg, S., and J. Herman: Panoramic mosaic by manifold projection. In Proc. *Computer Vision Pattern Recognition*, pages 338–343, 1997.

Petty, R., M. Robinson, and J. Evans: 3d measurement using rotating line-scan sensors. *Measurement Science Technology*, **9**:339–346, 1998.

Reulke, R., and M. Scheele: Der Drei-Zeilen CCD-Stereoscanner WAAC: Grundaufbau und Anwendungen in der Photogrammetrie. *Photogrammetrie Fernerkundung Geoinformation*, **3**:157–163, 1998.

Sandau, R., and A. Eckardt: The stereo camera family waoss/waac for spaceborne/ airborne applications. *Int. Archives Photogrammetry Remote Sensing*, **XXXI(B1)**:170–175, 1996.

Šára, R.: The class of stable matchings for computational stereo. Technical Report CTU-CMP-1999-22, Center for Machine Perception, Czech Technical University, Prague, Czech Republic, 1999.

Seitz, S.M.: The space of all stereo images. In Proc. *Int. Conf. Computer Vision*, pages 26–33, 2001.

Shum, H.-Y., M. Han, and R. Szeliski: Interactive construction of 3d models from panoramic mosaics. In Proc. *Computer Vision Pattern Recognition*, pages 427–433, 1998.

Shum, H.-Y., and L.-W. He: Rendering with concentric mosaics. In Proc. *SIGGRAPH*, pages 299–306, 1999.

Shum, H., A. Kalai, and S. Seitz: Omnivergent stereo. In Proc. *Int. Conf. Computer Vision*, pages 22–29, 1999.

Shum, H.-Y., and R. Szeliski: Stereo reconstruction from multiperspective panoramas. In Proc. *Int. Conf. Computer Vision*, pages 14–21, 1999.

Southwell, D., J. Reyda, M. Fiala, and A. Basu: Panoramic stereo. In Proc. *Int. Conf. Pattern Recognition*, Volume A, pages 378–382, 1996.

Svoboda, T.: Central Panoramic Cameras Design, Geometry, Egomotion. PhD thesis, Czech Technical University, Prague, Czech Republic, 1999.

Szeliski, R., and S. Kang: Direct methods for visual scene reconstruction. In Proc. *IEEE Works. Representation Visual Scenes*, pages 26–33, 1995.

Wei, S. K., F. Huang, and R. Klette: Color anaglyphs for panorama visualizations. Technical Report, CITR-TR-19, Dept. of Computer Science, The University of Auckland, Auckland, 1998a.

Wei, S. K., F. Huang, and R. Klette: Three dimensional view synthesis from multiple images. Technical Report, CITR-TR-42, Dept. of Computer Science, The University of Auckland, Auckland, 1999a.

Wei, S. K., F. Huang, and R. Klette: The design of a stereo panorama camera for scenes of dynamic range. In Proc. *Int. Conf. Pattern Recognition*, Volume III, pages 635–638, 2002.

Wei, S. K., F. Huang, and R. Klette: Determination of geometric parameters for stereoscopic panorama cameras. *Machine Graphics & Vision*, **10**:399–427, 2002a.

Xu, G., and Z. Zhang: *Epipolar Geometry in Stereo, Motion and Object Recognition - A Unified Approach.* Kluwer, Amsterdam, 1996.

Zhang, Z., R. Deriche, O. Faugeras, and Q.-T. Luong: A robust technique for matching two uncalibrated images through the recovery of the unknown epipolar geometry. Technical Report 2273, INRIA, Lucioles, France, 1994.

Zhang, Z., and G. Xu: A general expression of the fundamental matrix for both perspective and affine cameras. In Proc. *Int. Joint Conf. Artificial Intelligence*, pages 23–29, Nagoya, Japan, August 1997.